Paper ID: KL-01

Desalination of Seawater: a Source of Freshwater

M N A Hawlader
Department of Mechanical Engineering, International Islamic University Malaysia,
Jalan Gombak, 53100 Kuala Lumpur, Malaysia
E-mail: mehawlader@iium.edu.my

Abstract

In this paper, a brief description of the major desalination processes currently in practice in different parts of the world has been presented. Although Multi-Effect Distillation (MED) was one of the first desalination processes, initially it went through some operational difficulties, which led to a decline of its use once Multi-Stage Flash (MSF) distillation was invented. MED is considered energy efficient but this was not the main concern, as the countries making use of MSF had their own sources of energy supply. MSF played a very strong role during the last fiftyyears in the conversion of seawater to fresh water. Recently, Reverse Osmosis (RO) method has been showing a great potential, and further developments of new membrane materials and pre-treatment processes are likely to reduce the cost of water production dramatically. With the increase of fuel prices, the energy cost has become important and MED has reappeared on the scene. The production cost of water from MED process is found less than MSF in certain cases. Cogeneration, water and power, and hybrid system are likely to be the future direction.

Keywords: *Desalination, multi-stage flash distillation, multi-effect distillation, reverse osmosis, performance, costs.*

1. Introduction

For the survival of mankind, water is considered one of the most important substances. Nature has provided earth with a large body of water; about 75% of the earth surface is covered with water. About 97% of the water available on earth is in the ocean and approximately 2% in glaciers and ice caps. Without adequate treatment, water in the ocean is not ready for human consumption. Nature provides cycle where enough supply of fresh water exists to meet the requirements of mankind. The distribution of fresh water is not uniform. There is a shortage of water in many parts of the world. This may be attributed to the growth of population, increased industrial activities, shortage of land areas and nature of climatic conditions.

All around the world, the demand for steady supply of fresh water will continue to grow and, very often, it does not match the supply. Hence, a sound water resources management and development will remain a constant challenge. In countries with a limited supply of fresh water, water management policy must be an integral part of national economic policy. Of the various solutions to fresh water problem, the conservation, purification and reuse, and identification of new resources should receive considerable attention [1].

The concept of desalination for the production of fresh water is not new, and this method of obtaining fresh water was used on board ships in the year, as early as, 1700 [2] to provide drinking water. The system was based on thermal distillation process making use of submerged tube design. Slowly land based desalination units begun to grow and the first one was built in Aden more than 100 years ago. Many small distillation plants, less than 0.5 mgd (million gallons per day), were installed in the Middle East in the early part of 1930 [3-4].

The technology has grown up steadily, and current desalination systems have massive capacities; some even designed to supply water for an entire state. For example, the Al Jubail II Complex in Saudi Arabia produces close to a million cubic metres (207.9 mgd) of fresh water per day.

There are several ways of classifying the desalination methods that have been employed over the years. These are as follows:

i) processes where seawater undergoes a phase change i.e. distillation, freezing;
ii) processes without phase change i.e. membrane method.

The distillation method is normally energy intensive and requires supply of thermal energy at temperature less than 120^{o}C. The waste heat from industrial processes and power plant may be used for distillation. Three methods, MSF, MED and vapour compression (VC), found wider applications in the Gulf States [2]. MSF has been widely used in

the Middle East for large-scale conversion of seawater to fresh water. In recent years, significant developments are taking place in MED and beginning to compete with MSF. MED is considered thermodynamically more efficient than MSF but it could not compete with MSF for a long time due to some operational difficulties. Also, its maximum unit capacity is limited compared with MSF.

The membrane method, on the other hand, does not require thermal energy but, normally, operates at high pressure [3-4]. Reverse Osmosis (RO) type of desalination, which was introduced in the Middle East about three decades ago, could not compete with MSF due to the quality of seawater, which required adoption of complex pre-treatments methods. Ever since, there have been considerable improvements in pre-treatment methods and membrane materials, and this method is likely to be competitive for any size of the plant. This method is considered efficient and, particularly, suitable for countries with limited land area. Several other methods are available for the conversion of seawater to fresh water such as electrodialysis, crystallization etc .

In this paper, MSF, MED and RO methods of desalination will be considered in a greater detail and their role in the development of large scale desalination plants will be discussed.

2. Methods of Desalination

There are several ways seawater [4-6] can be converted to fresh water. Actual nature would depend on the desalination method used. The process includes the following steps, as shown in Figure 1.

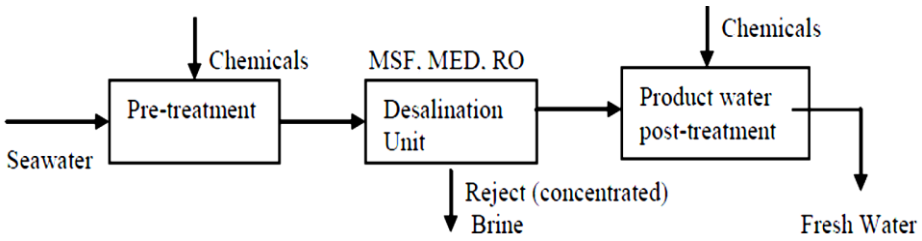

Figure 1. Schematic diagram of a desalination process [3].

The nature of pretreatment would depend on the type of nature intake system and the level of pollution around it. Seawater drawn from the ocean is cleaner and requires less pre-treatment.Pre-treatment of raw feed water is necessary to preserve the life and reliability of the desalination equipment [7].As mentioned earlier, there are a number of methods available for the conversion of seawater to fresh water. Irrespective of the method of conversion process, the product water should have a total dissolved solid (TDS) content of less than 500 ppm [5-6], as shown in Table 1.

Table 1. Typical constituents of seawater and potable water [5-6]

Constituents	Seawater (mg/L)	Potable Water (mg/L)
Barium	0.02	1.0
Calcium	412	75
Carbonates	28	150
Chloride	19500	250
Copper	$1x10^{-4}$	1.0
Fluoride	1.3	1.5
Iron	0.002	0.3
Lead	$5x10^{-7}$	0.05
Magnesium	1290	50
Manganese	$2x10^{-4}$	0.05
Mercury	$3x10^{-5}$	0.001
Nitrates/Nitrogen	11.5	10
Phosphates	0.06	0.4
Potassium	380	10
Silica	2	7.1
Sodium	10770	200
Sulphates	905	400
Total dissolved solid	33387 (ppm)	500 (ppm)
pH	8.0	6.5 - 8.5
Turbidity	3 - 15 NTU	5 NTU

Most widely used desalination processes areMulti-stage Flash(MSF),Multiple-effect Distillation(MED) and Reverse Osmosis(RO), as shown in Figure 2.

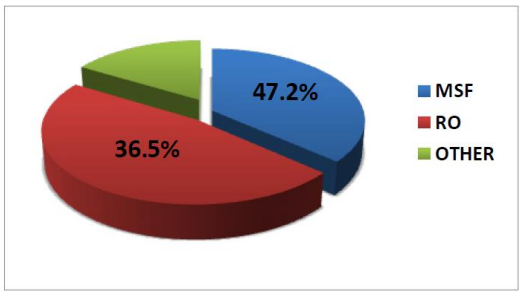

Figure 2.Contribution of different desalination processes[4]

2.1 Distillation method

This method includes two approaches: flash distillation or membrane distillation. Flash Distillation method may include Multi-stage Flash (MSF) or Multi-effect Distillation(MED).

2.1.1 MSF System

In MSF method, the saline water is heated to a higher temperature and passed through a series of chambers at decreasing pressure, as shown in Fig.3

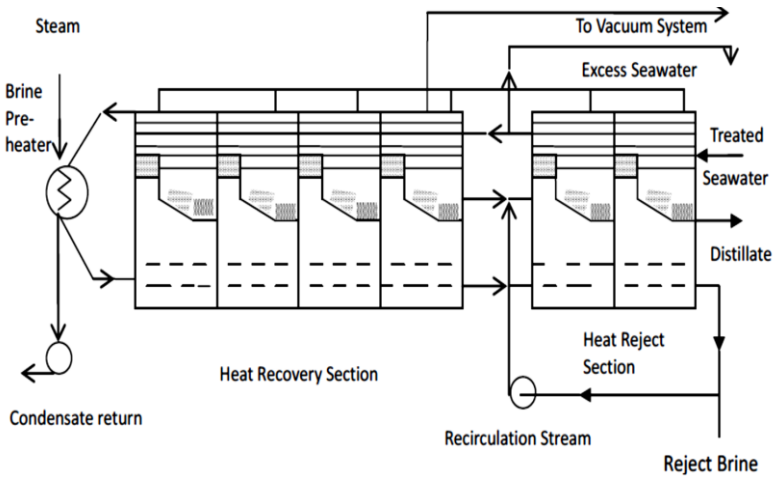

Figure 3. The MSF desalination process [4]

A brine heater heats up the sea water using low pressure steam available from cogeneration power plant [7], such as, a gas turbine with a heat recovery steam generator or from a steam turbine power plant. Then the seawater is fed on the tube side of the heat exchanger that is located on the upper portion of evaporator. Thus, the seawater heated by the condensing steam enters the evaporator flash chambers.Normally, there are multiple evaporators, typically containing 19–28 stages in modern large MSF plants. The top brine temperature (TBT) range is usually within 90 to 120ºC. To accelerate flashing in each stage, the pressure is maintained at a lower value than that in the previous stage.

2.1.2 MED System

The multi-effect distillation (MED) process is considered the oldest but a very efficient desalination method. In MED, the seawater undergoes boiling in multiple stages without supplying additional heat after the first effect. The evaporators are arranged either (a) horizontally [horizontal tube evaporator (HTE) with evaporated seawater sprayed outside the tube while the heating steam is condensed inside the tubes] or (b) vertically [long vertical tube evaporators (VTE) with boiling seawater falling film inside the tube while the heating steam is condensed outside the tubes] [6]. Figure 4 shows the schematic of an MED process. The MED specific power consumption is below

1.8 kWh/m^3 of distillate, significantly lower than that of MSF, which is typically 4 kWh/m^3.

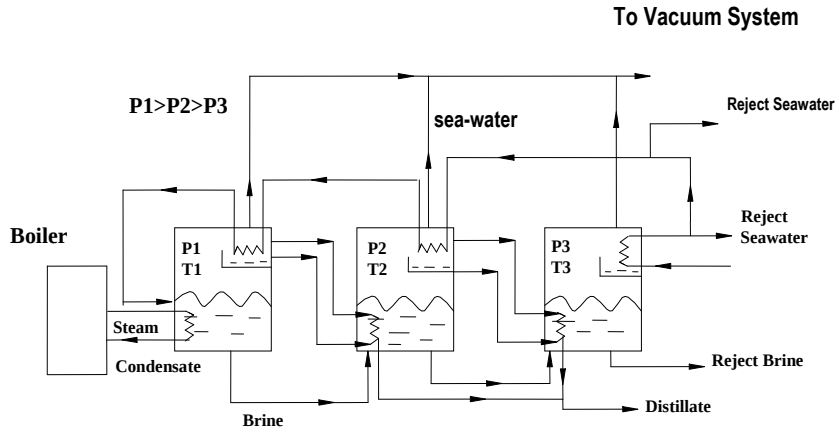

Figure 4. Multi-effect Desalination system

2.13 Reverse Osmosis (RO)

In the previous section, MSF, a distillation process involving extensive use of thermal energy has been discussed. RO, on the other hand, makes use of membranes, as shown in Figure 5, and it was developed in direct competition with distillation process. It's popularity lies in the fact that it requires no thermal energy and the plant is usually compact. For small countries, application of RO technology is likely to find greater appeal compared to other processes.

In the desalination of seawater using a selective membrane, one side of the membrane holds concentrated brine while the other contains nearly pure water. By applying a pressure on the concentrated brine, the pure water is prevented from permeating back into the brine side by osmosis. The pressure applied is higher than the osmotic potential, the difference in osmotic pressure across the membrane, and this results in not only preventing pure water permeating into brine solution but enables permeation of water out of the solution - the principle of reverse osmosis.

A basic RO plant includes a high pressure pump (HPP), the membrane module, and an energy recovery turbine (ERT). The function of the ERT is to extract hydraulic energy from the waste brine before it is discharged. The schematic diagram of a basic plant is shown in Figure 5.

Currently, different types of RO membranes are available [8] e.g. cellulose acetate, aromatic polyamide etc. These membranes typically consists of a relatively non-porous, dense surface layer approximately 0.1 -1.0 microns thick supported by a highly porous sponge-like substructure, which forms the bulk of the membrane. The cellulose acetate membrane was one of the first generation used for desalination. The aromatic polyamide membranes, commercially known as B9 and B10 permeators, are a relatively recent development by DuPont. A new generation of membranes have also been introduced recently, which utilize a wide variety of polymers. These composite membranes can operate over a wide range of pH and at temperatures of upto 50^{o}C. Some of the recent membranes are capable of separating 99%salt in a single stage. Recent membranes, spiral wound and hollow-fine fibre permeators, have shown better durability, larger flux and excellent separation performance.

In the desalination of seawater using RO, the HPP is used to increase the feed pressure to 50 - 70 atm. The reject brine from the RO membranes usually have a flow rate of 50% -70% of the feed flow and pressure of about 5 - 10 atm lower than the feed pressure. It contains a large amount of hydraulicenergy, which can be recovered using Pelton wheel impulse turbine, reverse running centrifugal pumps or direct drive turbine generators

The fouling of membranes is considered one of the difficulties to be overcome before it finds wider applications and further reduction in cost of desalinated water. Extensive research activities are underway to develop a pre-treatment method, such as ultrafiltration and microfiltration before the seawater feed is delivered to the RO permeators. Further development in membrane materials and pre-treatment methods will lead to a RO system, which is expected to be very much cheaper than what we have today.

3. Comparison of Desalination Processes

The comparison of different desalination methods can be made in two ways [6]: performance of the system and cost comparison. While evaluating the performance of desalination systems, the following factors should be considered:

i) ease of operation/ star-up/ shut-down;
i) complexity of process; and
ii) maintenance requirements.

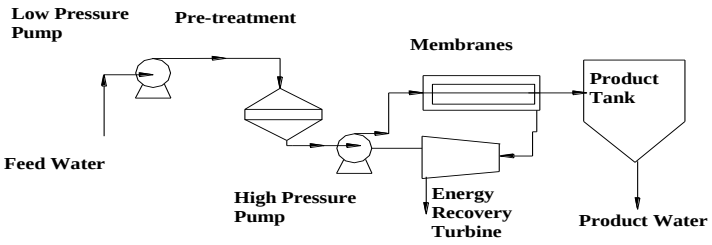

Figure 5. Reverse Osmosis (RO) system

Although there are significant differences in the degree of operational difficulties among the processes, the start-up time vary considerably among these processes. Generally, the RO plants show short start-up time, 0.5 - 1 hour, while MSF and MED plants have longer start-up time, 2 - 4 hours. The complexity of desalination processes depends on the controls, alarms, pumps and other auxiliary systems and skills of operating personnel. In this respect, the RO plants are considered least complex. As far as maintenance is concerned, RO plants require as much maintenance as other desalination processes.

While comparing the costs, the performance ratio, energy requirement, top brine temperature have also been considered [1,6,8-10]. Table 2 shows the investment cost, PR and energy requirements of the three processes considered in this study.

Table 2. Investment costs and performance comparison of different desalination processes

Process	MSF	MED	RO
Specific investment cost ($/m^3/day)*	1100 - 1600	900 - 1250	700 - 1000
PR(kg water/ 2326 kJ)	6 - 40	10 -15	30 - 100
Energy	Low pressure steam	Low pressure steam	Electrical
Top operating temperature	90 - 120^{o}C	90 - 115^{o}C	25 - 40^{o}C

* year 2000 figure

4. Closure

Three methods of desalination have been receiving considerable attention in recent years. Of the two distillation methods, MSF is extensively used in many parts of the world, including Middle East countries. This process is energy intensive and, with the increase in fossil fuel price, search for alternative method went on. There has been renewed interest in MED and it may offer an alternative to MSF. RO method of desalination is likely to make greatest impact with the development of new materials and pre-treatment processes. Cogeneration: power and water, and hybrid system, a combination of MSF and RO or MED and RO, are likely to be the solution of water shortage problem

5. References

[1] Malek, A., Hawlader, M.N.A. and Ho, J.C. Large -scale seawater desalination: a technical and conomic review. ASEAN J. Sci. Technol. Development Vol. 9 No.2.pp 41-61, 1992.

[2] Alawadhi, A.A. Desalination - where are we now? The International Desalination and Water ReuseQuarterly, Vol. 12 No.1, pp12 - 21, May/June 2002.

[3]Hawlader, M. N. A., Desalination of seawater: a solution to shortage of fresh water. Proc CAFEO 20: 20thConf of ASEAN Fed of Eng Org, 2 – 4 Sept 2002, Phnom Penh, Cambodia.

[4] Khan, A.H., Desalination processes and multi-stage flash distillation practice, Elsevier, New York, 1986.

[5] De Zuane, Hand book of drinking water quality: standards and controls, Van Nostrand Reinhold, New York, 1990.

[6] Seawater: It's composition, properties and behaviour, Prepared by an Open University Team, Walton hall, Milton Keynes, England, Pergamon Press, 1989.

[7]Mahbub, F., Hawlader, M.N.A. and Mujumdar, A.S., "Combined water and power plant (CWPP)-a novel desalination technology". Desalination and Water Treatment, 5(2009), 172-177.

[8] Finnegan, D.R. and Wagner, W.M.,Process selection guide to seawater desalting. Desalination, vol.38, pp137-145, 1981.

[9]Darwish M.A., Yousef F. A. and A1-Najem N.M., Energy consumption and costs with a multi-stage flashing (MSF) desalting system, Desalination, vol. 109. pages 285-302,1997.

[10]Moch, I. Jr., A 21st Century Study of Global Seawater Reverse Osmosis Operating and Capital Costs, Proceedings of the IDA World Congress and Water Reuse, March 8–13, Manama, Bahrain. 2002.

Paper ID: KL-02

A Review of Power Sector by Energy Types in SAARC Countries

Firoz Alam[1], Quamrul Alam[2]and Rashid Sarkar[3]

[1]School of Aerospace, Mechanical and Manufacturing Engineering
RMIT University, Melbourne, Australia
[2]Department of Management, Monash University, Melbourne, Australia
[3]Department of Mechanical Engineering, Bangladesh University of Engineering and Technology (BUET), Dhaka 1000, Bangladesh

Abstract

The member nations of the South Asian Association for Regional Cooperation (SAARC) are the home of over 1.65 billion people who are significantly lagging behind in economic and human development indices. The inadequate power generation and supply are considered to be the main hindrance. Limited indigenous energy resource of individual SAARC nation is not enough to generate sufficient power for the rapid economic development and industrialisation. Moreover, the availability of limited indigenous energy resources differs among SAARC nations. This study reviews the current power generation capacity of each member of the SAARC by energy type and their constraints. This study also highlights the need for a collective effort to develop mechanism for the utilisation of the limited resources available in SAARC region. Greater cooperation among SAARC nations is emphasised to overcome regional energy shortages and enhance collective energy security.

Keywords: Energy, power, energy security, coal, gas, hydro resource, SAARC, power trade

1. Introduction

South Asian Association for Regional Cooperation (SAARC) comprising Afghanistan, Bangladesh, Bhutan, India, Maldives, Nepal, Pakistan, and Sri Lanka has a population of 1.65 billion which makes it one of the densely populated landmass of the world.The fast growing economies of SAARC nations have led to an increase consumption of energy and power resulting in growing demand for energy resources. Thus, for the energy security of SAARC nations emanates from the growing imbalance between the demand for energy and its supply from indigenous sources resulting in increased import dependence [16, 22, 31]. The drain on national resources to meet energy import is a major economic, political and social issue in the entire SAARC region[22, 31].

The SAARCnations are highly dependent on imported energy especially crude oil and petroleum products. The imports range from 25% of commercial energy consumption in the case of Bhutan to 100% in the case of Maldives[21]. Sri Lanka and Maldives do not possess any indigenous fossil fuel sources while India, Pakistan and Bangladesh have limited indigenous fuels (gas & coal). However, all SAARC nations face mounting energy import bills.India is the 4th largest energy consumer in the world after China, USA and Russia[1, 3,10, 16]. India's primary energy consumption is: crude oil (30%), natural gas (8%), coal (55%), nuclear energy (2%), hydro-electricity (4%), and others (1%). In 2013, India's net imports were nearly 144.3 million tons of crude oil, 16 milliontonnes of oil equivalent (Mtoe) of LNG and 95 Mtoe coal totalling to 255.3 Mtoe of primary energy which was equal to 42.9% of the total primary energy consumption [1, 6, 8, 14, 19-20, 22, 24, 26, 28]. By 2030, India's dependence on energy imports is expected to exceed 53% of the country's total energy consumption[22].

The growth of electricity generation in India has been hindered by domestic coal shortages[22, 26, 28] and as a consequence, India's coal imports for electricity generation increased by 18% since 2010[8, 22, 26].There is no significant amount of fossil fuel reserves in Nepal, Bhutan, Sri Lanka and Maldives except small quantity coal reserves in Bhutan.. The power generation in Maldives and Sri Lanka is largely dependent on imported liquid fuel while in Nepal and Bhutan is primarily based on hydro resources. Afghanistan, Bangladesh and Pakistan's power generation is primarily dependent on local and imported fossil fuel. Nevertheless, Pakistan, Bhutan and Nepal have enormous hydro resources potential to generate a large percentage of power.

According to the International Energy Agency (IEA) projection, the energy demand in SAARC nations would grow at more than the double of the world over the next several decades [1, 3, 21-22, 26, 28].

The oil consumption growth rate is expected to be around 6% in all SAARC countries. India with 5,700million barrels has the highest crude oil reserves in South Asia [1]. In comparison, Pakistan and Bangladesh have 341 million barrels and 28 million barrels respectively. At current level of production, India is projected to exhaust its crude oil reserves in 30 years unless new reserves are discovered [21-22].

As part of energy security consideration, the resources required to generate power (electricity) should be taken into account. The power is considered a secondary form of energy, obtained partly from the primary energy sources (coal, gas, and liquid fuel) directly though conversion. The increasing demand for powerindicates the economic activities,industrialisation and improvement of living standards. Power plant development is highly capital-intensive and hence large scale public funding is required for the expansion of power generation capacity [6, 8, 26, 28]. Therefore, the primary objective of this paper is to review the current power generation situation in each SAARC nation especially the types of fuel source currently they use to generate power and bilateral and multilateral cooperation in power generation to enhance the energy security.

2. Power Generation in SAARC Nations

2.1 India

India has installed power generation capacity of 277,710 MW as on 31 August 2015 which makes India the world's 5th largest power generator [1, 6, 8, 16-17]. Out of this, nearly 39% is from state owned power plants, 32% is from privately owned power plants and 29% is from centrally owned power plants. The private sector involvement in power generation in India is notable (29%) [6, 8]. The state wide power generation by energy sources is shown in Table 1.

India's energy demand has been growing rapidly due to the rise of industrial growth and household consumption. However, the demand has been outstripped by the demand. Most power generation in India from fossil fuels (mainly coal) as shown in Table 1.

Table 1: State wide power generation by source in India, adapted from [6, 8, 14]

Power Generation in India as of July 2015								
		Coal MW	Gas MW	Hydro MW	Nuclear MW	Others MW	Total MW	Population million
1	Maharastra	24,669	3,476	3,332	690	6,206	38,373	112.4
2	Gujarat	16,010	6,806	772	559	4,802	28,950	60.4
3	Madhya Pradesh	11,126	257	3,224	273	1,670	16,551	72.6
4	Chhattisgarh	13,193		120	48	327	13,688	25.6
5	Goa	326	48		26		400	1.5
F	Dadra & Nagar Haveli	44	27		8		80	0.4
G	Daman & Diu	37	4		7		48	0.3
	Central - Unallocated	*1,622*	*197*		*228*		2,047	
6	Rajasthan	9,401	825	1,719	573	4,711	17,229	69.0
7	Uttar Pradesh	11,678	550	2,168	336	990	15,722	200.0
8	Punjab	6,445	289	3,145	208	503	10,590	27.8
9	Haryana	6,528	560	1,457	109	139	8,792	25.4
A	Delhi	5,002	2366	822	122	35	8,347	12.0
10	Himachal Pradesh	152	62	3,422	34	729	4,398	6.9
11	Uttarakhand	400	69	2,442	22	244	3,177	10.2
12	Jammu & Kashmir	329	304	1,805	77	157	2,672	12.6
B	Chandigarh	33	15	62	9	5	124	1.1
	Central - Unallocated	*977*	*290*	*754*	*130*	8835	10,986	
13	Tamil Nadu	10,075	1026	2,182	987	4787	19,057	72.2
14	Karnataka	6,408		3,600	476	2020	12,504	61.2
15	Andhra Pradesh	5,849	1673	1,722	127	83	9,454	49.5
16	Telangana	5,598	1698	2,013	149	439	9,896	35.2
17	Kerala	1,039	534	1,882	229		3,682	33.4
C	Puducherry	249	33		53		335	1.3
	Central - NLC	100					100	
	Central - Unallocated	*1,523*			*300*		1,824	
18	West Bengal	12,974		1,248		131	14,354	92.0
19	Odisha	6,753		2,167		117	9,037	42.0
20	Bihar	2,516		129		114	2,760	103.8
21	Jharkhand	6,777	83	147		20	7,027	33.0
22	Sikkim	92		174		52	318	0.6
	Central - Unallocated	*1,572*					1,572	
23	Assam	187	719	430		34	1,369	31.2
24	Tripura	19	539	62		21	641	3.7
25	Meghalaya	18	105	357		31	510	3.0
26	Arunachal Pradesh	12	43	98		105	258	1.4
27	Manipur	16	68	81		41	206	2.7
28	Nagaland	11	46	53		30	140	2.0
29	Mizoram	10	38	34		36	119	1.1
	Central - Unallocated	*38*	*104*	*127*			269	
D	Andaman & Nicobar					50	50	0.4
E	Lakshadweep					1	1	0.1
	Islands					51	51	
	Total	169,809	22,855	41,750	5,780	37,515	277,710	1,208

Five states out of 29 generate most power in India. Figure 1 illustrates the leading power generating states. The state of Maharashtra is at the top position with installed power generation capacity (38,373 MW) in India. The state of Gujarat is on second position with 28,950 MW of installed power generation capacity followed by Tamil Nadu (19,057 MW), Rajasthan (17,229 MW) and Madhya Pradesh (16,551 MW).

The state wise population of these five states are: 112.4, 60.4, 72.2, 69 and 72.6 million respectively. It may be noted that Maharashtra, Gujarat and Tamil Nadu are highly industrialised. Therefore, their electricity demand is also higher than other states.

India has large renewable energy sources especially solar, wind and hydro energy to generate power. It is currently the 10th largest wind power generator in the world.

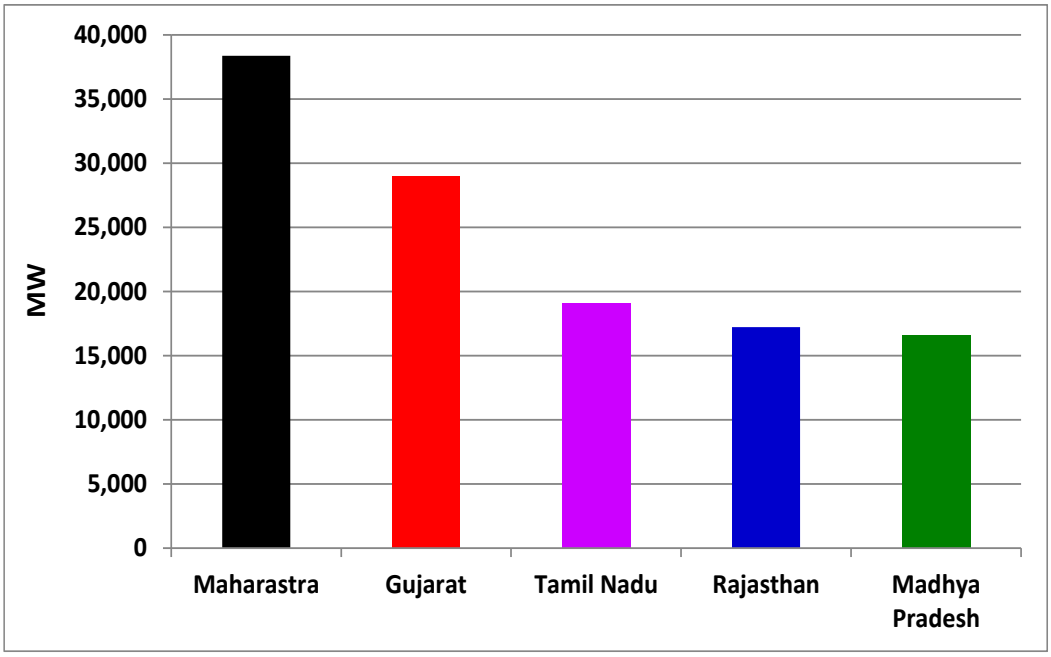

Figure 1: Top five power generating Indian states

2.2 Pakistan

The 2nd largest power generator of SAARC nations is Pakistan after India. Its current installed power generation capacity is approximately 23,000 MW [4, 11, 23]. However, the demand has significantly been outstripped the generation capacity (28%). Pakistan's power generation is dominant by the state owned company 'Water and Power Development Authority (WAPDA)' for all over Pakistan except the city of Karachi[10]. According to the International Energy Agency (IEA) forecast,the total power demand would be around 50,000 MW by 2025 in Pakistan[23,27, 30].

The power generation by energy types in Pakistan is shown in Table 2. Pakistan's power generation portfolio has been well diversified: hydro (29%), coal (23%), imported oil (23%) and nuclear (6%). Pakistan has the highest hydro resource potential to generate power over 60,000 MW [30]. At present, the power generation in Pakistan has been facing severe shortage of energy as the gas reserve is almost exhausted. Despite having enormous potential for hydro power generation, Pakistan heavily relies on imported fuel (23%). In the next 10 years, peak electricity demand is expected to rise by 5% per annum, which is roughly 1,500 MW [4, 11, 17]. It is interesting to note that Pakistan has the highest ratio of power generation from nuclear energy (6%) among all SAARC nations. Figure 2 shows the location of power plants by fuel type across Pakistan.

Table 2: Power generation by source in Pakistan, adapted from [4, 11, 27, 30]

Power Generation in Pakistan						
Coal	Gas	Hydro	Nuclear	Others	Total	Population
MW	MW	MW	MW	MW	MW	million
5,239	4,245	6,611	1,322	5,152	22,569	192

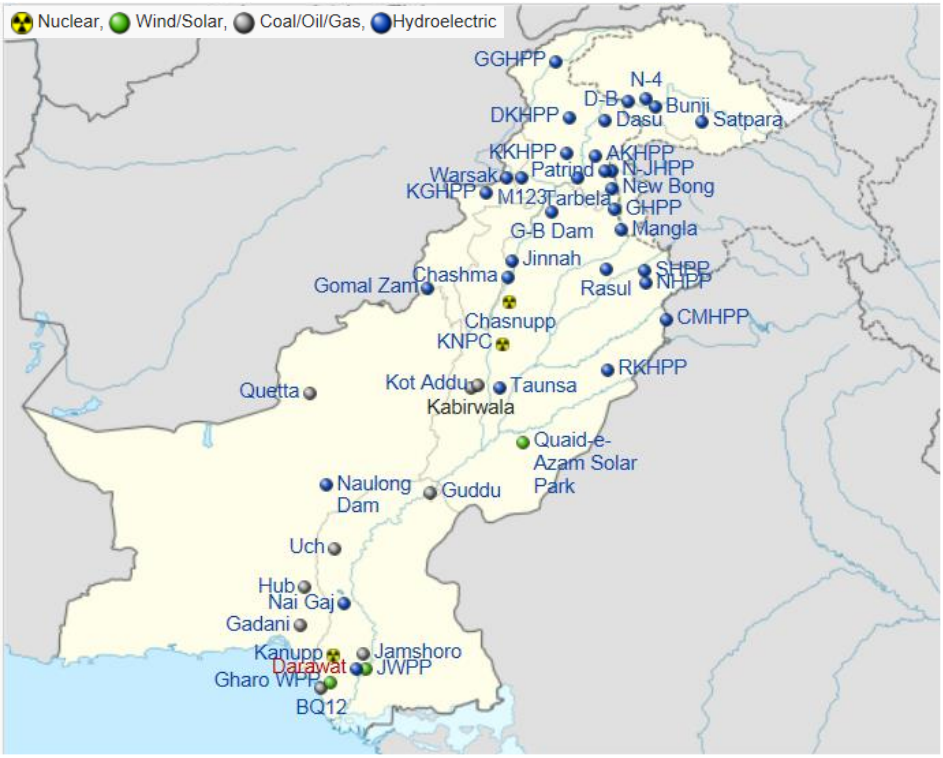

Figure 2: Distribution of Pakistan's power plants across the country, adapted from [11, 27]

2.3 Bangladesh

Bangladesh is the 3rd largest power generator among SAARC nations after India and Pakistan. The installed generation capacity is around 12,000 MW out which state owned companies produce approximately 8,000 (67%) and remaining by public private partnership (PPP) and rental (33%). Bangladesh also imports 500 MW power from neighbouring India using 400 kV DC transmission line through Baharampur (India)-Bheramara (Bangladesh) corridor [7,18, 31-32].

Bangladesh has limited fossil fuel resources. It generates power overwhelmingly by natural gas (~70%). The remaining ratio constitutes imported fuel (26%), indigenous coal (2%) and hydro (2%). As the current gas reserve is depleting rapidly, Bangladesh wants to diversify its fuel mix by lowering the dependency on indigenous gas. The government of Bangladesh allowed private sectors to generate power based on mainly imported liquid fuel. This change in the fuel mix of power generation has significant implications on power generation cost and national public subsidy. The use of liquid fuel especially the high-speed diesel and furnace oil has increased power generation cost from around US$ 0.03 per kWh in 2008 to US$0.07 in 2012 [10, 21, 31].

The power generation based on fuel type in Bangladesh is shown in Table 3.At present, Ghorasal thermal power plant is Bangladesh's largest power plant with the general capacity of 950 MW. Most power plants in Bangladesh are small scale however larger power plants are currently being built in southern Bangladesh. These power plants will be fuelled by imported coal and LNG. A nuclear power plant with the capacity of over 2,000 MW is currently being under construction in the central western Bangladesh which is expected to be operational by 2019 [31-32].

One of the important achievements of Bangladesh power sector is the ability to reduce the system loss. It has managed to lower the system loss to around 11% in 2015 from 24% in 2002 [18]. Major power plants and power transmission across nation are shown in Figure 3.

Table 3: Power generation by source in Bangladesh, adapted from [18, 31-32]

Power Generation in Bangladesh as of October 2015						
Coal	Gas	Hydro	Nuclear	Others	Total	Population
MW	MW	MW	MW	MW	MW	million
250	7,474	230	0	3,923	11,877	160

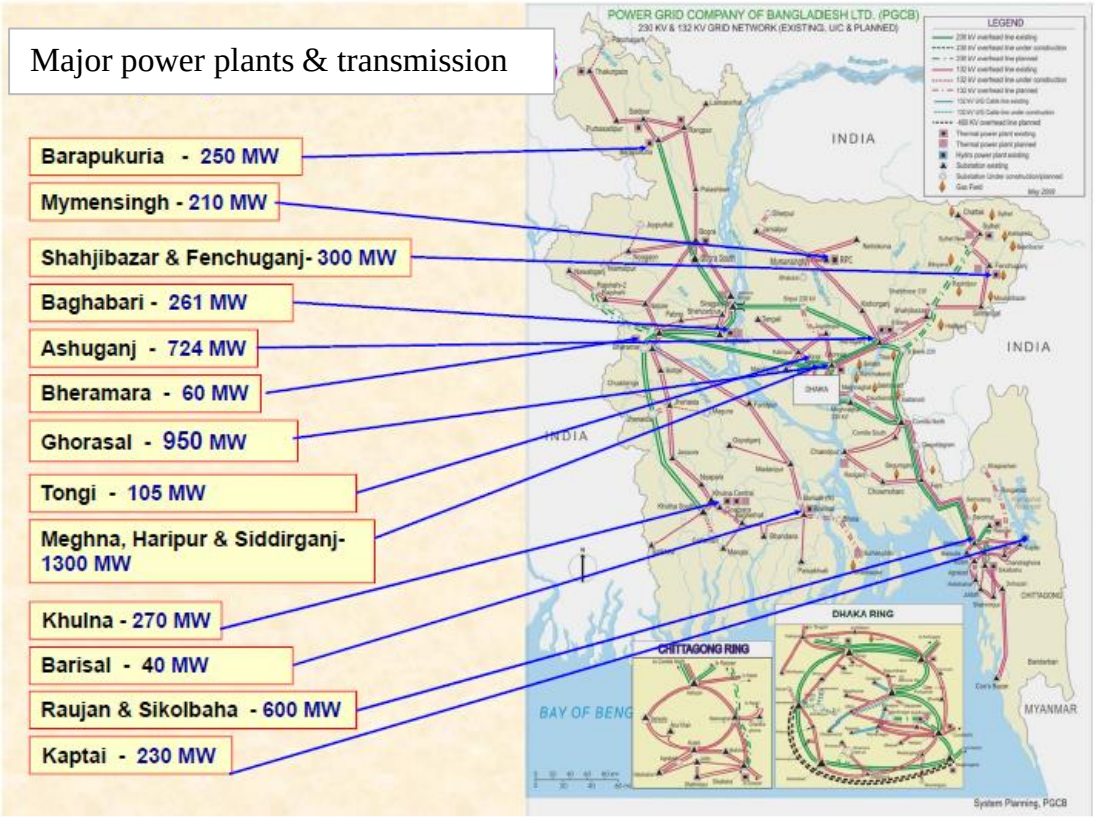

Figure 3: Major power plants and power transmission grids in Bangladesh, adapted from [18, 31-32]

2.4 Nepal, Bhutan, Sri Lanka, Afghanistan and Maldives

Nepal currently generates around 800 MW power mainly from hydro resources. Like Bangladesh, the state owned company 'Nepal Electricity Authority (NEA) is the main generator and distributor of power across Nepal [15, 21]. It owns 28 small scale hydro power plants with the total generation capacity of 480 MW. Additionally, Nepal has 33 Independent Power Produces (IPP) who generate around 230 Megawatts. NEA also generates 90 MW power by using two liquid fuel operated power plants [15, 21]. With the expanding economy, the demand for power has also increased. As a result Nepal faces severe power shortages especially during the dry season. Nepal's power generation by fuel types is shown in Table 4.

Table 4: Power generation by source in Nepal, adapted from [1, 15, 21]

Power Generation in Nepal as of Jan 2015						
Coal	Gas	Hydro	Nuclear	Others	Total	Population
MW	MW	MW	MW	MW	MW	million
		710	0	90	800	28

Currently Nepal imports around 50 MW power from India through the Muzaffarpur (India) – Dhalkebar (Nepal) 400kV transmissionline. Thelength of this high voltage transmission line is 125km of which 86.43kmis in India and 39 km is in Nepal [15, 22].

Nepal has a huge hydropower potential. It has approximately 40,000 MW of economically feasible hydropower potential. However, at present it generates approximately 700 MW of hydropower [15, 22, 31]. Despite having huge hydropower resources, only about 40% of Nepal's population has access to the grid power. Most of the power plants in Nepal are run-of-river type with energy available in excess of the in-country demand during the monsoon season and deficit during the dry season.Nepal's major power infrastructures are shown in Figure 4.

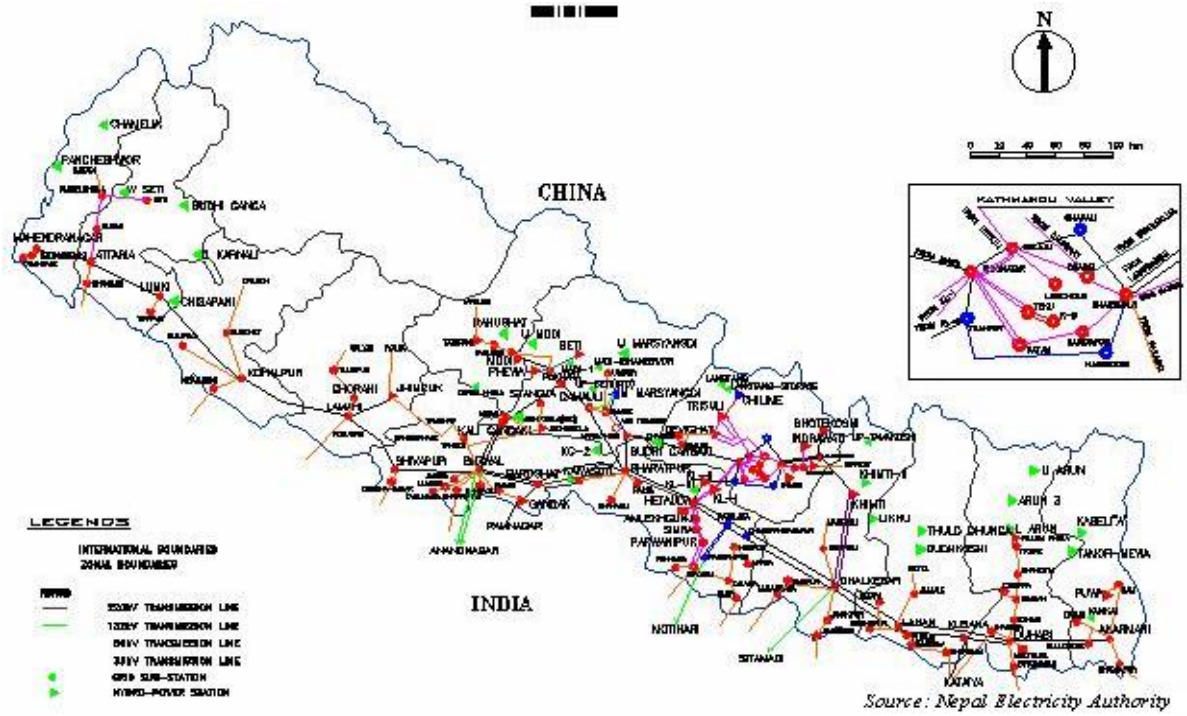

Figure 4: Major power plants and transmission lines in Nepal, adapted from [15]

Like Nepal, Afghanistan is a mountainous and land-locked country located in Central Asia bordering with Iran, Pakistan, Afghanistan, Tajikistan and China. At present, Afghanistan generates approximately 840 MW power mainly from hydro resources (~600 MW) and remaining gas (240 MW). Power generation by fuel type in Afghanistan is shown in Table 5.Afghanistan has enormous hydropower potential (over 25,000 MW) [1, 3, 13].

Table 5: Power generation by source in Afghanistan [1, 3, 13]

Power Generation in Afghanistan as of Jan 2011						
Coal	Gas	Hydro	Nuclear	Others	Total	Population
MW	MW	MW	MW	MW	MW	million
0	240	600	0	0	840	33.00

Sri Lanka's total power generation capacity is nearly 4,000 MW primarily from hydro resources (over 1,665 MW), liquid fuel (1,395 MW) and gas (440 MW) and the remaining power from wind and solar resources [1-3, 5, 21].Thermal power plants in Sri Lanka roughly match the installed hydropower generation capacity, with a share of nearly 42% of the total available capacity as of December 2013 and 45% of power generated by liquid fuel, gas and coal [1-3, 5, 21]. Sri Lanka possesses good micro hydro resources and wind resources which can be used to enhance the percentage of power generation by non-fossil fuel resources. Current Sri Lanka's power generation by fuel type is shown in Table 6.

Table 6: Power generation by source in Sri Lanka, adapted from [1-3, 5, 21].

Power Generation in Sri Lanka as of Jan 2012						
Coal	Gas	Hydro	Nuclear	Others	Total	Population
MW	MW	MW	MW	MW	MW	million
300	440	1,665	0	1,535	3,940	22.00

Bhutan currently generates around 1,490 MW but it has a large hydropower potential at around 24,000 MW [1, 9, 12]. Twenty eight (28) power plants ranging from 8 kW to1,020 MW contribute to Bhutan's total power generation. It may be noted that only 6% of its potential is currently being utilised. India plays a major role in Bhutan's hydropower development. It provides finance and technical know-how to Bhutan to build hydropower

plants, and purchases most of the power generated (~ 75%). At present, the power export constitutes over 40% revenues and 25% of Bhutan's GDP.The hydropower infrastructure and wheeling charge provides another 25% of the nation's GDP [1, 9, 12].

According an agreement signed by Bhutan and India in 2006, India agreed to import at least 5,000 MW of power from Bhutan. In a revised agreement in 2009, India agreed to financially support hydropower capacity development of 10,000 MW by 2020, and import all the surplus power from Bhutan [1, 9, 12, 22]. This has encouraged Bhutan to undertake 10 mega power development projects. Three main power projects are: a) 1,200 MW Punatsangchu-I, b) 1,020 MW Punatsangchu-II and, c) 720 MW Mangdechhu. These plants are currently under construction and expected to be operation by 2017. Other plants such as 600 MW Kholongchhu, 540 MW Amochhu Reservoir project, 570 MW Wangchu Run-of-the-River project, 180 MW Bunakha Reservoir project, 2640 MW Kuri Gongri Reservoir project, 770 MW Chamkharchhu-I HEP (Hydro-Electric Power) project and 2560 MW Sankosh Reservoir project are under construction at different stages [9, 12].The Bhutan's power generation landscape will significantly change in 2018 and beyond once all power plants will be operational. Nevertheless, Bhutan's current power generation is completely hydro based as shown in Table 7. It may be noted that Bhutan has no petroleum or natural gas reserves. However, it has some 1.3 million tonnes of coal reserve from which it currently extracts around 1,000 tonnes each year for domestic use. Bhutan also imports liquid fuel at some 1,000 barrels per day [12, 22]. Most liquid fuel is used for automobiles. Bhutan exports power to India using a 75 km long 400 kV DC lines. The power plants and transmission infrastructures of Bhutan are shown in Figure 5.

Table 7: Power generation by source in Bhutan, adapted from [1, 3, 9, 12, 22]

Power Generation in Bhutan as of Jan 2015						
Coal	Gas	Hydro	Nuclear	Others	Total	Population
MW	MW	MW	MW	MW	MW	million
		1,488	0		1,488	0.75

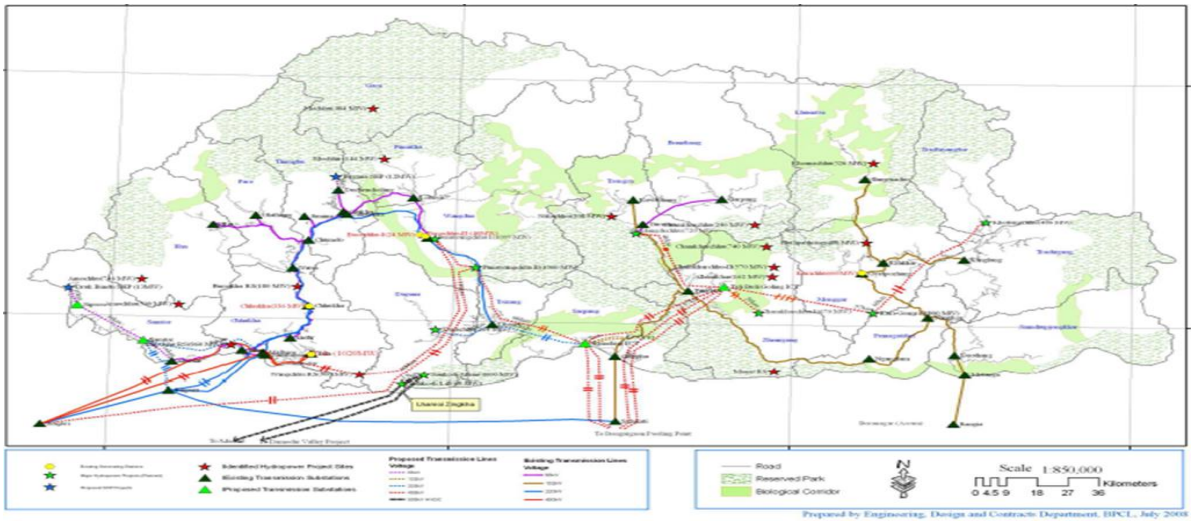

Figure 5: Major power plants and power transmission lines in Bhutan, adapted from [9,12]

Maldives is a tiny country of 0.4 million people which consists of 26 major atolls and 1,190 tiny islands (200 are inhabited). Only 33 islands have an area greater than 1 km^2. The total land area is around 300 km^2. However, the country has large sea area. Hence its total territory is over 859,000 km^2. Maldives does not have any indigenous fossil fuel. Its power generation is mainly achieved from liquid fuel (diesel). It currently generates around 140 MW (see Table 8) of which around 40% is generated by the State Electricity Company (STELCO) [25, 29]. Most power (~50 MW) is generated and consumed in the capital Male and its surrounding islands [25]. The Outer Islands – comprising 200 inhabited islands and 100 island tourism resorts. The inhabited islands have generation capacity collectively a total of 20 MW. Tourist islands are all privately operated and have their own independent power plants which make around a further 70 MW of power. A large scale wind project (20 MW) has been planned for the Male area. In addition, a 3.7 MW thermal power plant based on municipal waste is currently under construction in Male [25, 29].

Table 8: Power generation by source in Maldives, adapted from [21, 25, 29]

Power Generation in Maldives as of Jan 2015						
Coal	Gas	Hydro	Nuclear	Others	Total	Population
MW	MW	MW	MW	MW	MW	million
0	0	0	0	140	140	0.40

3. Regional Power Trading among SAARC Member Nations

The power generation varies from low 0.02 kW/person in Nepal to high 1.98 kW/person in Bhutan. The demand for the grid connected power is growing at around 10% per annum in most countries of the SAARC region. Overall, the per capita power generation and consumption in SAARC countries are extremely low compared to other Asian regions. A comparative power generation in SAARC nations is illustrated in Figure 6. As far as the total generation is concerned, India is the leader followed by Pakistan and Bangladesh (see Figure 7). However, all these three countries are facing severe shortage of generation capacity due to insufficient indigenous energy sources and funds. On the other hand, 30 to 40%populations of these countries have no access to grid connected power. Figure 8 clearly shows a very low per capita power generation especially in Bangladesh. Bhutan has the highest per capita power generation followed by Maldives and India. However when taken into account the total power generation and population, India has achieved a significant progress in power generation capacity and providing access to the populace. Despite India's low per capita generation of power (3rdafter Bhutan and Maldives in the SAARC region), it is going to achieve surplus power generation by 2017 provided its own coal production and transport infrastructure are developed adequately and undertaken coal and LNG import to meet the shortfall of indigenous energy resources [22].Currently India exports power to Bangladesh (500 MW) and Nepal (50 MW) and imports excess power from Bhutan.

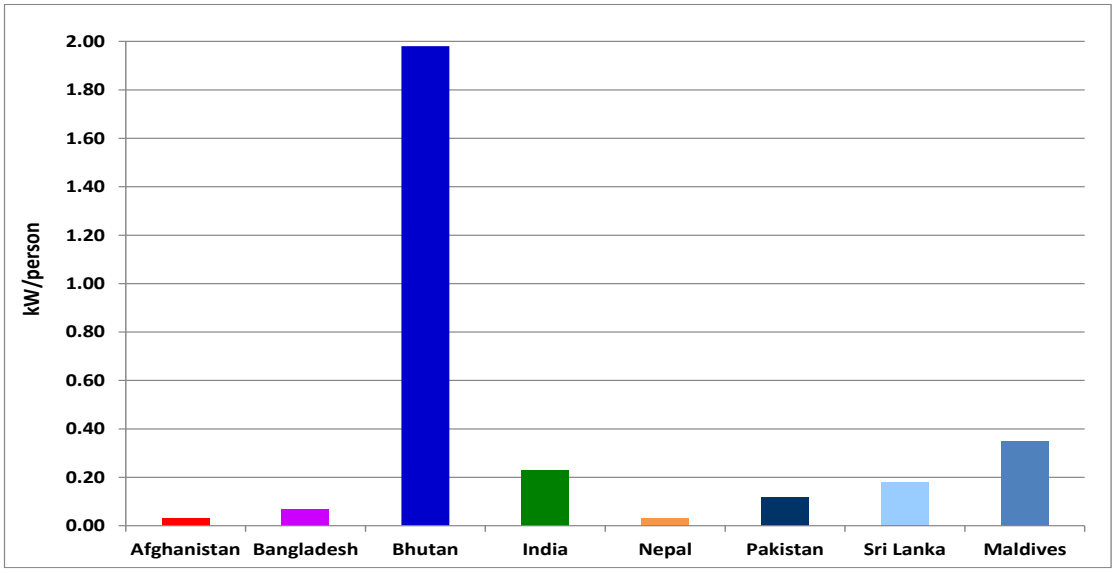

Figure 6: Per capita power generation in SAARC nations

As a remote and small nation, it is not feasible for Maldives to be grid connected with other SAARC nations and play a meaningful role in promoting regional cooperation in energy and power sectors. Nevertheless, Maldives can greatly benefit from the regional cooperation in the development of renewable energy technologies especially solar and wind as it has good wind resources and ample sunlight.

Bangladesh, Myanmar and Pakistan are extractingnatural gas which is predominantly used for the power generation. Bangladesh, Myanmar and Pakistan produce 55 million cubic metres per day (mcmd), 9 mcmd and 118 mcmd out of which 20 mcmd, 1.4 mcmd and 34 mcmd are consumed for electricity generation respectively [22]. Instead of burning the gas for power generation, Bangladesh, Myanmar, Pakistan and India can use the gas for industrial needs (fertilizer, cement, metallurgical plants). There is huge opportunity for mutually beneficial trading in energy resources among SAARC nations.

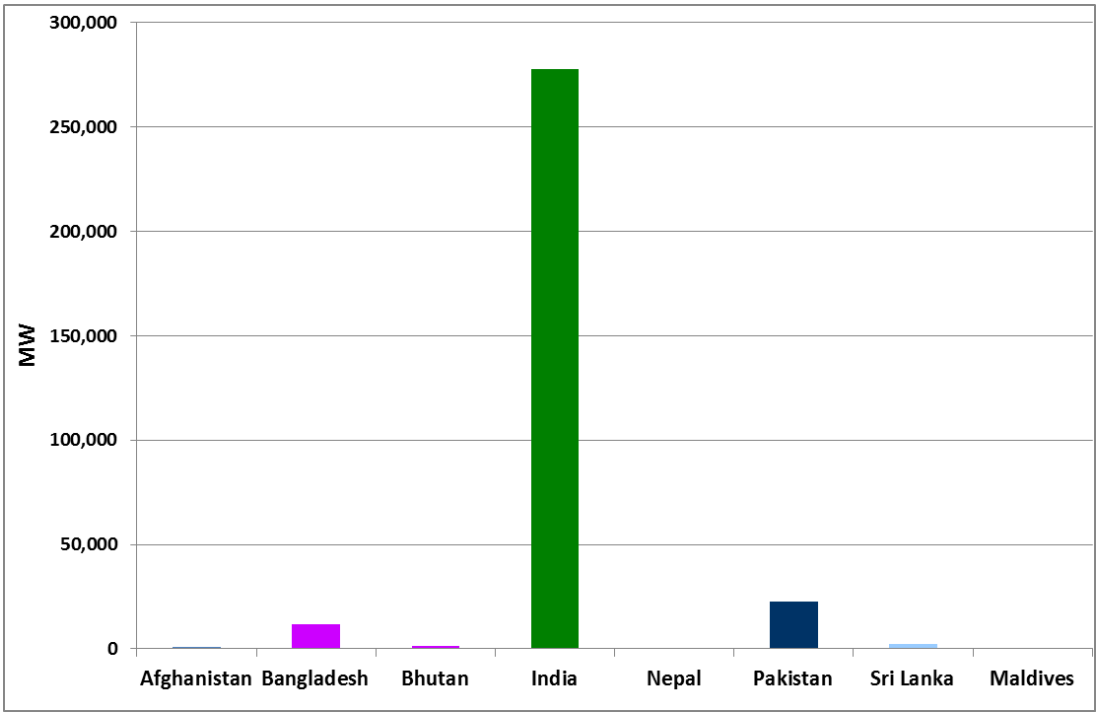

Figure 7: Country specific total power generation in SAARC nations

India, Bangladesh, Nepal, Bhutan, Pakistan, Afghanistan and Myanmar can work together to tape the huge hydro resources in Bhutan (24,000 MW), Nepal (40,000 MW), Afghanistan (25,000 MW) and Pakistan(60,000 MW).Recently India, Bangladesh, Nepal and Bhutan have signed an energy and power sector cooperation agreement which allows the signatories jointly invest in power plant development and trade surplus power among the signatories. This will usher in a new era for usingthe untapped hydro resources for power generation both in Bhutan and Nepal. India being the largest and Bangladesh - the 3rd largest economies in SAARC region both countries are in a position to purchase surplus power from the hydro based power plants in Bhutan and Nepal. In return, both Nepal and Bhutan can economically be benefitted not only via the revenues from power export but also getting access to sea via Bangladesh and India. It is worthy to note that India, Bangladesh, Nepal and Bhutan are now connected through the power transmission grids which need to be upgraded for large quantity power trading. Other remaining SAARC nations especially Pakistan, Afghanistan can connect directly with Indian national power grid and Sri Lanka can join Indian national grid via an undersea cable link which will then allow all SAARC countries grid connected except Maldives. There is ample opportunity for SAARC nations led by India in securing their energy requirements for power generation and economic uplifting of over 1.65 billion people.

4. Concluding Remarks

The power generation capacity in SAARC nations varies significantly. India is the leader. India and Sri Lanka have diversified their power generation by using a good mix of energy resources (coal, gas, hydro). India has further diversified using nuclear energy. In contrast, Pakistan and Bangladesh are heavily dependent on natural gas. In particular, Bangladeshdependence on natural gas over 80% of its power general poses a significant risk to its national development as its gas reserves are depleting very fast.

Bhutan is the leader in utilising renewable hydro resources for its entire power generationamongthe SAARC nations. Nepal and Bhutan should capitalise their vast hydro resources for power generation.

Maldives being a country of multiple atolls, it needs to depend on fossil fuel but it can explore wind and solar energy for micro scale utilisation in sparsely located atolls and islands which are not feasible to be grid connected.

Regional power trading among SAARC nations will strengthen energy security and economic prosperity of 1.65 billion people. It will also enhance mutual trust, economic and cultural cooperation.

India and Bangladesh need to invest in hydro power developments in Bhutan and Nepal as they (India and Bangladesh) can be the sole importer of surplus power from these two countries (Nepal and Bhutan).

The transmission loss of power will be minimal if the surplus power from Bhutan and Nepal is consumed in Bangladesh and north-eastern part of India due to the close geographical proximity.

References

1. BP Statistical Review of World Energy 2014 & BP Statistical Review of World Energy 2015, http://www.bp.com/content/dam/bp/pdf/energy-economics/statistical-review-2015/
2. Ceylon Electricity Board Statistical Digest, 2013
3. Cherp, A. and Jewell, J. (2014), The concept of energy security: Beyond the four As, *Energy Policy*, Vol. 75, 415-421
4. Dawn Newspaper, Pakistan, http://www.dawn.com/news/1172656
5. Economic and Social Statistics of Sri Lanka 2013 pp. 58
6. Energy Statistics 2015, Issue 21, Central Statistics Office, Ministry of Statistics and Programme Implementation, Government of India, New Delhi, pp. 1-103, www.mospi.gov.in
7. GSI Report, March 2014, Geneva, Switzerland, pp 1-22, https://www.iisd.org/gsi/sites/default/files/ffs_bangladesh_agenda.pdf
8. India Energy Security Scenarios 2047 (IESS 2047), NITI Aayog, Government of India, http://www.indiaenergy.gov.in/
9. International Rivers report "Mountains of Concrete", http://www.internationalrivers.org/files/attached-files/ir_himalayas.pdf
10. Jonsson, D.K., Johansson, B., Mansson, A., Nilsson, L.J., Nilsson, M. and Sonnsjo, H. (2015), Energy security matters in the EU Energy Roadmap, *Energy Strategy Reviews*, Vol. 6, 48-56.
11. Pakistan Today (2015), LNG: The whole truth in Pakistan, 30 April www.pakistantoday.com.pk/2015/04/30/
12. Long Term Plan For Water Supply Infrastructures (2012), Ministry of Works & Human Settlement Department of Engineering Services, Government of Bhutan. June. Page 11
13. Ministry of Energy and Water, Afghanistan Government, http://mew.gov.af/en/
14. Ministry Power, Government of India, http://powermin.nic.in/
15. Nepal Electricity Company, http://www.nea.org.np/
16. Newberry, D. (2007), Power Reforms. Private Investment and Regional Cooperation In: Ahmed, S. and Ghani, E.(Eds.), South Asia: Growth and Regional Integration, WorldBank,Washington D.C.
17. Page, K. (2003), Asia & Pacific Review 2003/04: The Economic and Business Report, Asia and Pacific Review (21 ed.) (Kogan Page Publishers), ISBN 0-7494-4063-5
18. Power Cell, Ministry of Power, energy and Mineral Resources Bangladesh, http://www.powercell.gov.bd/index.php?page_id=267
19. Rasul, G. (2014), Food, water, and energy security in South Asia: A nexus perspective from the Hindu Kush Himalayan region, Environmental Science & Policy, Vol. 39, 35-48.
20. Real Time Energy Production and Consumption, 'World energy consumption clock', US energy debt clock, www.usdebtclock.org/energy
21. Sankar, T.L., Raza, H.A., Barkat, A., Wijayatunga, P., Acharya, M. and Raina, D.N. (2010), Energy Security for South Asia, USAID's South Asia Initiative for Energy (SARI/Energy). www.sari-energy.org
22. Singh, B.K. (2014), South Asia energy security: challenges and opportunities, Energy Policy, Vol. 63, 458-468.
23. The Tribune Newspaper, Pakistan, http://tribune.com.pk/story/208495/dark-days-ahead-electricity-woes-to-worsen-in-future
24. The world Fact book: Energy Sections of Pakistan, Burma, Bangladesh, Nepal, Bhutan & Sri Lanka, Retrieved 17 February 2013.
25. UNDP Report (2007): Energy and Poverty in the Maldives.
26. US Energy Information Administration (EIA): India Energy Profile, http://www.eia.gov/beta/international/
27. Wikipedia, https://en.wikipedia.org/wiki/List_of_power_stations_in_Pakistan
28. Yep, E. (2011), India's Widening Energy Deficit, The Wall Street Journal, 3 September, 2011
29. SREP Investment Plan, Republic of Maldives (2012), 7 February, pp. 1-92
30. AAJ TV Report: http://aaj.tv/2015/03/pakistan-has-hydropower-potential-to-generate-60000-mw-electricity-asif/
31. Khan,I., Alam, F. and Alam, Q. (2013), The global climate change and its effect on power generation in Bangladesh, Energy Policy, Vol. 61: 1460–1470
32. Bangladesh Power Development Board (BPDB), http://www.bpdb.gov.bd/bpdb

Ultraprecision Manufacturing through Revolutionary Innovation

Mustafizur Rahman
Department of Mechanical Engineering, National University of Singapore,
9 Engineering Drive 1 Singapore 117575, mpemusta@nus.edu.sg

Abstract

In recent years, the trend in miniaturization of products has been pervasive in areas such as information technology, biotechnology, environmental and medical industries. Micro-machining is the key supporting technology that has to be developed to meet the challenges posed by the requirements of product miniaturization and industrial realization of nanotechnology. Micro-machining techniques can be carried out by techniques based on energy beams (beam-based micro-machining) or solid cutting tools (tool-based micro-machining). Beam-based micro-machining has some limitations due to poor control of 3D structures, low material removal rate and low aspect ratio. Moreover, these processes require special facilities and the maximum achievable thickness is relatively small. Some of these limitations can be overcome by tool-based micro-machining techniques using ultra precision machine tools and solid tools used as cutting elements to produce the micro-features with well controlled shape and tolerances. In this paper, an attempt has been made to present the recent development contribution in tool based micro/nano machining process from National University of Singapore.

1. Introduction

Tool-based micro-machining techniques essentially include precision machining processes such as turning, milling, grinding and electrical discharge machining (EDM), whereby material removal is done at the micron level. The advantages of such processes are that almost every material such as metals, plastics and semiconductors can be machined with no limitation for high aspect ratio. On the contrary, microstructures produced by photolithography have the limitations of low aspect ratio and quasi-3D structure [1, 2]. It is possible to fabricate high-aspect-ratio components with submicron structure by Lithographie Galvanoformung und Abformung (LIGA) process (from the German – a combination of lithography, electroplating, and molding process) using the synchrotron radiation process and focused ion beam (FIB) machining process. However, present laboratory-scale and industrial fabrication techniques using LIGA require special and extremely expensive facilities like a synchrotron system and require machining of expensive masks which has imposed a hindrance on quick and economical fabrication of microparts. Furthermore, the dimensional ranges that such processes cover are sometimes not required which is illustrated in Fig. 1[3]. It can be observed from the figure 1 that tool-based micromachining has a unique place for performing micromachining operations at the lower boundary of micromachining range (between 5 μm and 50 μm) to bridge the gap between mechanical machining, photolithography, and LIGA process for dimensional range and aspect ratio [4, 5].

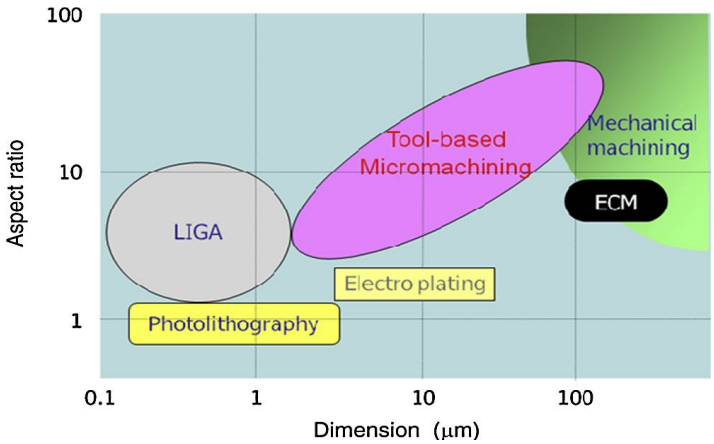

Figure 1: Illustration on dimensional range and aspect ratio of several machining processes. [3]

The major drawback of the tool based process is the limit of machinable sizes, however, some limitations of machinable sizes can be overcome through hybridized/Compund machining process. In order to achieve meaningful implementation of compound micro-machining techniques three important areas are required to be addressed. These are: development of machine tools capable of performing compound micro-machining (i.e. micro turning, micro milling, micro EDM, etc. on the same machine and setup), understanding of process physics to provide relevant background for modeling, measurement, identification of control parameters and application of feedback control in order to control compound and hybrid manufacturing processes and development of compound and hybrid processes. An integrated effort in these areas is needed for successful implementation of tool-based micro-machining, which can only be achieved through a paradigm shift in thoughts and processes conventional machining. This shift can be materialized only through revolutionary innovation rather than evolutionary one. In this paper, the development contribution in micro/nano-machining based on solid tools (tool-based micro/nanomachining) in National University of Singapore are highlighted. In the area of micromachiningachievements in the development of machine tools for combined/hybrid micromachining, machining process development integrating few tool based approach like micro-EDM, micro-EDG, micro-ECM, micro-turning and micro grinding to produce miniature parts/patterns is presented. In the area of nano machining process success in the development of machine tools to achieve economical nano surface generation, machining techniques from image to surface patterning, development of a novel cutting process named as Synchronized Tool and Roller (STR) diamond for direct diamond turning of radial frensel lens structures on a roller mould, and recent research in the area of ductile mode machining of brittle materials is presented.

2. Compound and Hybrid Micro/Nano Machining

In recent years, compound and hybrid micromachining has become the most promising technology for the production of miniaturized parts and components. This technology is becoming increasingly more important and popular because of a growing demand for industrial products, with an increased number not only of functions but also of reduced dimensions, higher dimensional accuracy, and better surface finish. Compound and hybrid machining is the combination of processes and/or machines to produce parts in a more efficient and productive way [6]. In NUS our research in compound and hybrid machining is divided into two major areas including development of machine tools for compound and hybrid micromachining, development of machining process for compound and hybrid micromachining.

2.1. Development of Machine Tools for State-of-the-art Compound and Hybrid Micro Machining

Although micromachining is the key supporting technology that has to be developed to meet the challenges posed by the requirements of product miniaturization, in many cases a single micromachining process cannot fulfill all of the requirements due to the limitation of that process.One of the main difficulties in compound micromachining is the availability of an appropriate machine tool that can be used for the development of compound and hybrid micromachining processes. Most machine tools capable of nonconventional machining are not designed to perform conventional machining processes. Furthermore, most of the machine tools do not facilitate the measurement of fabricated products on machine, which has the potential to be used as feedback and to compensate tool trajectory online. Another constraint is imposed by the precision required for such fabrication, which most conventional computer numericalcontrol (CNC) machine tools cannot fulfil. Mechanical and thermal deformation, chatter vibration, tooling, and its clampingusually constrain making small, super precise parts with large, conventional machines. Ultra-precision machines that provide a highdegree of motion accuracy are extremely expensive and mostly do not include facilities for compound processes. Therefore, the firstand the most important requirement for the development of compound and hybrid machining processes is the development ofa multipurpose machine tool or the integration of facilities for performing two or more manufacturing processes in one single setupand platform. In order to achieve effective implementation of compound and hybrid micromachining techniques, four important areas need to be addressed as shown in the Fig. 2 below[7]

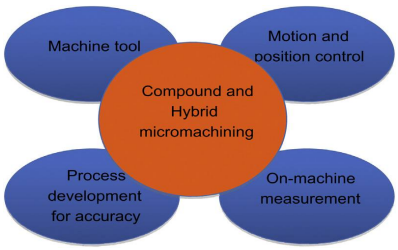

Figure 2: The technologies required for successful development of compound and hybrid micromachining processes.[8]

To meet the above mentioned requirements, World's First Integrated Multi-Process Machine Tool for Micro Machining is developed in National University of Singapore (Machine Model: DT – 110). Multiple types of micro machining, e.g., micro turning, micro milling, micro EDM, micro ECM, etc. can be carried out on the same machine (Fig. 3). This highly flexible machine ensures high rigidity for precision machining. Some of the special features of the developed machine: (a) Miniature machine design, (b) Low noise and low heat generation, (c) High resolution with full feedback (resolution of 0.02 µm and accuracy of +/-1.0 µm) and (d) Capable of handling multiple processes, µ-EDM, µ-ECM, µ-Milling, µ-Turning and µ-Drilling. This technology is Patented and Licensed to Mikrotools Pte Ltd, a Spin-off company of National University of Singapore.

Figure 3: World's First Integrated Multi-Process Machine Tool for Micro Machining. (Machine Model: DT – 110). [7]

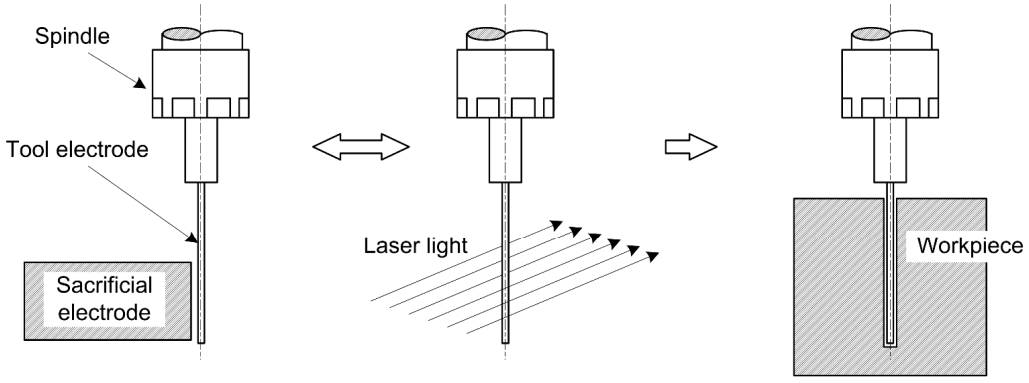

(a) On machine tool electrode fabrication by micro EDM

(b) On machine optical measurement

(c) Fabrication of high aspect ratio micro structure by EDM

Figure 4: Micro EDM with on-machine tool fabrication, and on machine tool inspection steps in DT – 110 machine.[9]

2.2. Development of Innovative Compound and Hybrid Micro Machining Process

Usually, if a manufacturing engineer is asked to fabricate a micro shaft that is50 µm in diameter and 10 mm in length, engineer will argue that it is impossible. The usual reasons why such a narrow shaft cannot be machined are insufficient stiffness of the product which will deflect due to the cutting force because the engineer will think only of a turning process from the free end of the blank up to the desired length by longitudinal turning and in this process these dimensions cannot be achieved. However, engineers tend to forget that both the problems of deflection and cutting force can be taken care of applying the fundamental engineering knowledge. As shown in equations (1) and (2) they can control the deflection by calculating the step size for which will ensure that even a 50 µm shaft will be able to withstand the deflection without yielding. If step turning is carried out as shown in Fig. 5a – Path B instead of Path A, it can be easily performed. Machined shafts are shown in Fig. 5b[4].

Deflection, $\delta = \frac{Fl^3}{3EI} = \frac{64Fl^3}{3\pi E d^4}$ ….. (1) Bending stress, $\sigma = \frac{32Fl}{\pi d^3}$ …… (2)

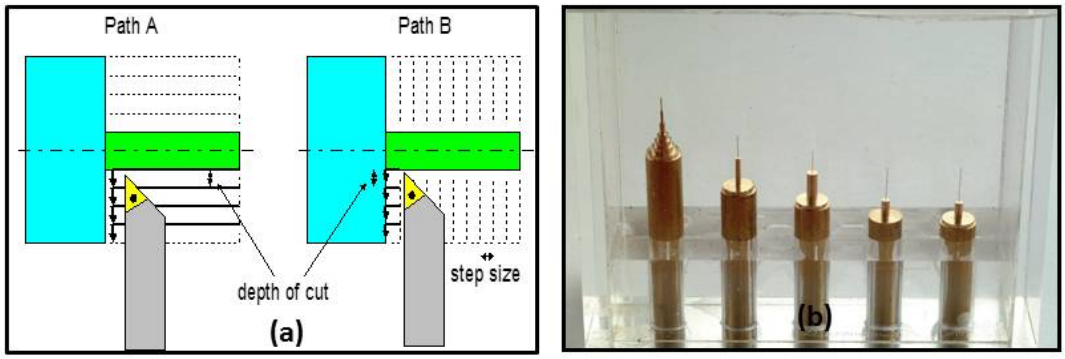

Figure 5: (a) Two possible ways to do turning, (b) Micro Shafts of diameter 50 microns[[4]

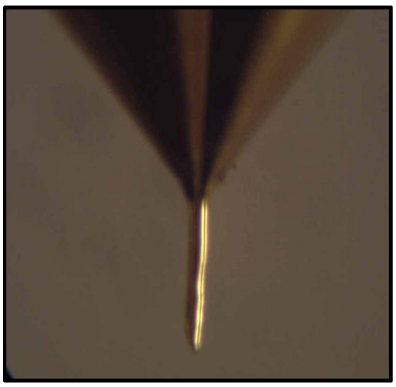

Figure 6: Bending of micro shafts in conventional turning

Although Step cutting force could be applied to control the deflection in a certain range, in conventional machining full straight shaft below 100µm diameter is difficult to achieve. However, through hybrid machining deflection can be controlled up to very narrow diameter (5µm).This section presents some of the hybrid machining process innovations in NUS.

2.2.1. Micro-EDM and Micro Turning

Micro turning has the capability to produce three-dimensional (3D) structures on a microscale. The major drawback of the micro turning process is the limit of machinable sizes and the fact that the cutting forces influence machining accuracy. It is very difficult to achieve straight shaft below 100 mm diameter, and in many cases the tool either breaks or starts to wobble due to excessive radial cutting force on the micro shaft. Therefore, a compound process has been developed[10] where the commercial cutting tool is modified using the micro-EDM process to reduce the force component responsible for breaking of the shaft.

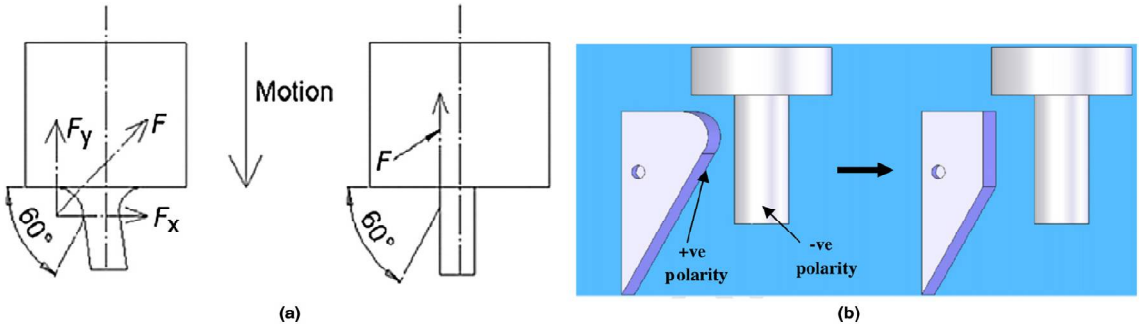

Figure 7: (a) Modification of a conventional cutting tool using the micro-EDG (variant of micro-EDM) process; and (b) a schematic representing the compound process combining modification of a cutting tool by micro-EDM and turning of a micro shaft by a modified tool tip.[10]

This compound process is the combination of micro-EDM and micro turning in a single setup. First, a commercially available polycrystalline diamond (PCD) tool is modified by the micro-EDG process to reduce the nose radius of the cutting tool, thus minimizing the force component that causes shaft deflection during micro turning. Commercially available PCD inserts, designed for a light finishing cut, have a relatively large tool nose radius (e.g., 100 μm). This tool nose resolves the cutting force on the shaft into two components, namely F_x and F_y, as can be seen in Fig. 7(a). The F_y component of the cutting force does the actual cutting, while the F_x component causes deflection of the micro shaft. A commercially available PCD insert is modified using the micro-EDG process to achieve a very sharp cutting edge, so as to reduce the F_x component of the cutting force significantly. This modification of the cutting tool makes it possible to achieve a straight shaft of much smaller diameter. The compound process combining micro-EDG and micro turning is presented schematically in Fig. 7(b). A dual-cutter setup is arranged for micro turning, one with a round nose for initial turning up to 100 μm, then a sharp tool for a final cut up to 20 μm.

After the micro turning process, the fabricated microelectrodes are used in machining of small and higher aspect ratio micro holes by micro-EDM on the same machine (Fig. 8). Therefore, this compound process is in fact a combination of three steps-

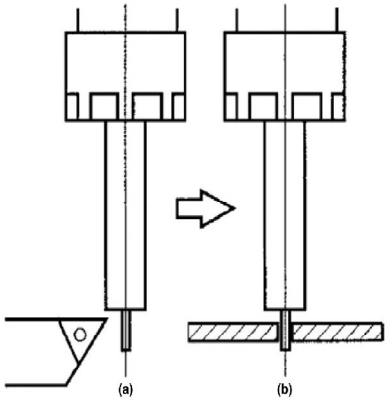

Figure 8: Compound process of fabricating a microelectrode using micro turning and applying a fabricated microelectrode in the micro-EDM drilling.[11]

Modifying the cutting tool using micro-EDG, fabricating micro shafts using micro turning, and applying fabricated shafts in micro-EDM drilling. Fig.9 illustrates the concept of the micro turning–micro-EDM compound machining process. An electrode of required dimension is first fabricated by micro turning prior to micro-EDM . Using this compound process, clamping error can be avoided, and deflection of electrode can be minimized; consequently, the accuracy of machining can be improved. The fabricated microelectrode and machined micro holes using the microelectrode are presented in Figure 9(a) and 9(b), respectively.

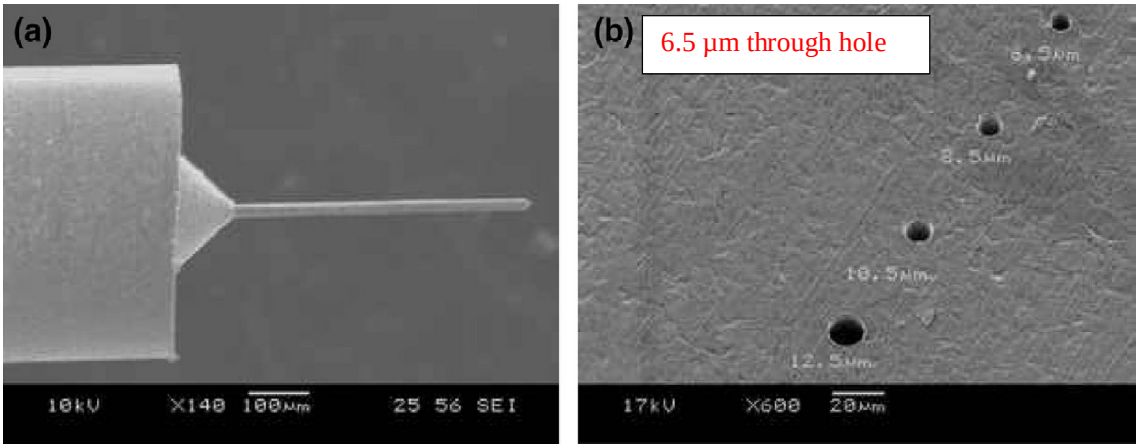

Figure 9: (a) A 19 mm graphite electrode of 0.5 mm length fabricated by a micro-EDG–micro turning compound process; and (b) fabricated micro holes (up to 6.5 µm hole in 50 µm plate) through hole with the microelectrode obtained by the micro turning–micro-EDM drilling compound process. [7]

2.2.2. Micro-EDM and Micro Grinding

The fabrication of a miniaturized (sub-100 µm) grinding tool for difficult-to-cut materials like PCD and tungsten carbide (WC) is necessary for machining of microchannel with improved surface finish. The micro-EDM process is found to be capable of machining any difficult-to-cut materials down to the desired dimension. Therefore, a compound process is developed[10] to solve the issues by combining the micro-EDM process with the micro grinding process. In this compound machining process, a PCD tool is fabricated on a machine in a desired shape using the block micro-EDG process. The PCD tool contains randomly distributed protrusions of diamond particles with dimensions around 1 µm that serve as the cutting edges for micromachining on glass. When the dimension of the PCD tool is reduced to the required dimension of the grinding tool by the micro-EDG process, the binder materials (usually nickel or WC) are removed because they are conductive, thus protruding the diamond particles, which are nonconductive. PCD with a cobalt binder, which can be shaped with micro-EDG, is emerging as a tool material for micro grinding of hard and brittle materials. The cobalt binder provides an electrically conductive network that can be removed with EDM. The diamond cutting edges are exposed as the discharges erode away the cobalt binder. Fig.10 shows the different steps of the micro-EDM–micro grinding compound process with a machining example in BK-7 glass. As can be seen from Figure 10(c) and 10(d), the fabricated slot has a very fine and smooth surface, which is comparable to the surface obtained from ductile mode cutting of glass in macroscale.

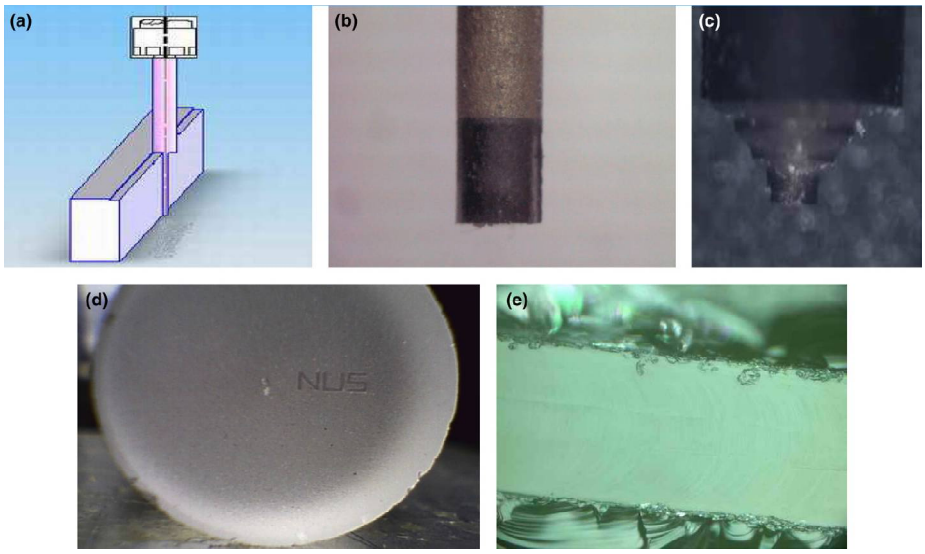

Figure 10: (a) A schematic diagram showing the block micro-EDG process (a variant of micro-EDM); (b) a PCD tool before the micro-EDG process; (c) fabrication of a micro grinding tool with the micro-EDG process; (d) micro channels on glass machined by the micro grinding process with a fabricated PCD tool; and (e) surface finish of the microchannel in glass. [10]

2.2.3. Simultaneous EDM and ECM Process (SEDCM)

With the ceaseless demand towards smaller, thinner and lighter products, much innovation has been made in macro-machining for micro and nano applications. Among these processes, micro-EDM and micro-ECM have the advantage of negligible cutting force due to the non-contact nature of the processes. Notwithstanding this advantage, each process has some undesirable effects which limit its capability. By appropriate combination of these two processes, their adverse effects could be significantly mitigated. However, micro-EDM operates in non-conductive dielectric fluid whereas micro-ECM employs conductive electrolyte. Due to these divergent requirements, micro-EDM and micro-ECM are usually used sequentially. This requires the repetitive change of machine tool or machining fluid hindering its practical use for micro-machining. Hence, to overcome the aforementioned issues a process combining micro-EDM and micro-ECM is developed in NUS[12] to achieve improved performance on both surface finish and dimensional accuracy. This hybrid machining process is named as Simultaneous Micro-EDM and Micro-ECM (SEDCM).To resolve the machining fluid issue, low resistivity deionized water was used, which has both characteristics of a conductive fluid and a dielectric fluid. In addition, short voltage pulses are also applied to localize material dissolution zone for higher precision. By examining the effect of different pulse parameters, it is found that pulse-on time is the main factor affecting the effectiveness of localization or suppression of material dissolution. Material removal phenomenon of micro-EDM in low-resistivity deionized water is then investigated. It is observed that there is a conversion from mere micro-EDM to hybrid micro-EDM/ECM (SEDCM) when the federate is reduced.

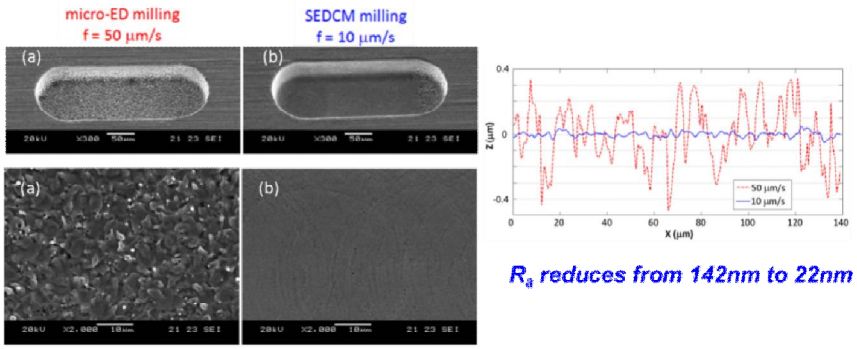

Figure 11: Simultaneous EDM and ECM (SEDCM) Process Carried out in each cycle (EDM during on-time and ECM during off-time) to improve the surface finish to mirror finish (Machine Model: DT – 110). [12]

SEDCM was applied to milling to fabricate intricate 3D micro-shapes with enhanced surface finish and dimensional accuracy. Micro shapes with surface roughness as low as 22nm Ra have been obtained as shown in Fig 11. For predicting suitable machining conditions for SEDCM milling, an analytical model is proposed and developed which can indicate critical conditions for transitions of micro- EDM/SEDCM/micro-ECM milling in low-resistivity deionized water.

3. Diamond turning

Ultra precision machining using single point diamond tool (SPDT) is a technique which removes materials from a few microns to sub-micron level to achieve ductile mode machining on hard-to machine materials such as electroless-nickel plating, silicon, quartz, glass and ceramics with no subsurface defects. Diamond turning machines are often equipped with fast tool servo (FTS) for its advantages in surface finish, precision level .In FTS-Diamond turning area research in NUS is divided into two major areas including machine tools development for FTS - diamond turning, development of innovative machining process using diamond turning.

3.1. Development of Ultraprecision Lathe

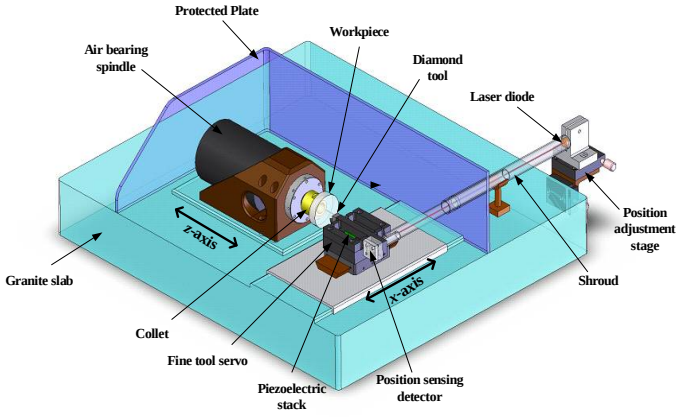

Figure 12: FTS- High speed diamond turning machine. (UPL –Series)[13]

The trend in ultra precision machining is such that surface finish and form error requirements are moving towards the nanometer level and submicron level respectively. Over the years, a lot of development has taken place in the machine tool industry for ultra precision machining whereby the resolution of machine movement has reached one nanometer. The challenge of making an affordable ultra precision machine tool has not been adequately addressed, and no significant research has been carried out in this area. Hence, a project was initiated to design, develop and fabricate a highly affordable ultra precision machine tool in NUS[13]. This is to be achieved by incorporating a fast/fine tool servo (FTS) system on a precisionmachine that is to be designed and fabricated using mainstream components at low cost. A high speed and low cost desktop ultra precision lathe has been developed. It features a high speed aerostatic work spindle of 15,000 rpm in a T-base 2-axis system mounted on a granite base. The arrangement of the machine components and elements are as shown in Fig. 12. Piezoelectric actuator which can actuate forward and backward in very high resolution is used to drive the FTS system in the *z*-axis direction. The FTS developed has been applied for waviness errors compensation in ultra precision lathe.

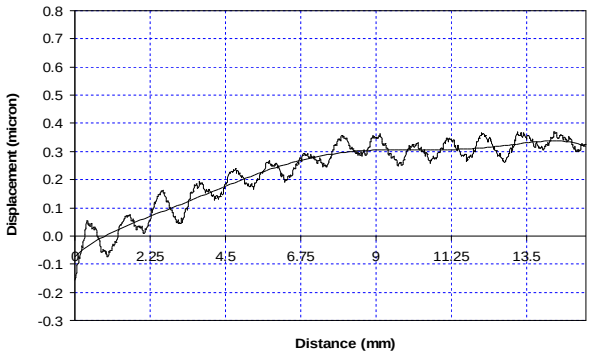

Figure 13: Machining profile of brass workpiece with and without fine tool servo compensation.[13]

A position sensing detector (PSD) is integrated in the FTS design, which is able to measure the straightness error of the translational stage accurately in real-time. For better tracking performance, proportional-integral (PI) feedback controller was implemented and tested in this study.

3.2. Development of Innovative Machining Process for Diamond turning

Conventional FTS diamond Turing process is not capable of machining steep circular grooves on the roller, due to their fixed tool–workpiece relative position and limited degrees of freedom.Moreover, in conventional FTS diamond Turing process fabrication of freeform surfaces is a tedious job due to the requirement of mathematical models based on non-uniform rational basis spline (NURBS). To resolve these issues new machining techniques using FTS diamond Turing process has been developed in NUS.

3.2.1. Development of Synchronized Tool and Roller (STR) Diamond machining

A radial Fresnel lens is an optical component which has a wide variety of applications, e.g., advanced lighting systems and concentrated solar power systems, due to its light weight, small size and excellent optical performance. It is able to realize light collimation and concentration with much less lens materials compared to a conventional spherical lens by collapsing the continuous surface profile of the spherical lens onto a plane.

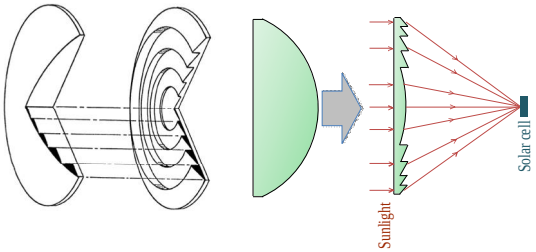

Figure.14: Use of Radial Fresnel lens for light concentration

Radial Fresnel lenses are usually fabricated by ultra-precision diamond machining , or by plastic injection moulding. Roll-to-Roll (R2R) embossing provides an advanced solution for continuous manufacturing of various optical films such as brightness enhancement film, lenticular diffuser film, and linear Fresnel lens film. Through utilizing high-precision roller moulds patterned with micro/nano surface structures, R2R embossing is able to replicate such structures onto flexible film substrates with significantly higher throughput and lower cost compared to conventional injection moulding technology [14, 15]. In general, the roller moulds applied in R2R embossing of optical films should be prepared by ultra-precision diamond machining, in order to achieve high profile accuracy and mirror-like surface finish of the machined feature. But a radial Fresnel lens is comprised of a series of central-symmetric steep circular grooves. So, direct diamond turning of radial Fresnel lens structures on a roller mould was considered infeasible, due to their fixed tool–workpiece relative position and limited degrees of freedom. So, none of the existing technique was not capable of machining steepcircular grooves on the roller. Fig. 15 schematically describes the incapability of ultra-precision diamond turning approach in generating radial Fresnel lens structures on a roller. The dark shaded zone represents the portion where the work material cannot be removed due to the steep circular groove profiles and the fixed cutting angle.

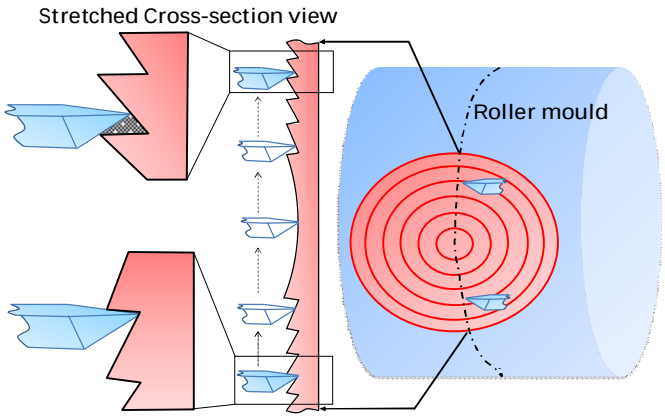

Figure. 15. Incapability to machine radial Fresnel lens on a roller using ultra-precision diamond turning method.[16]

A novel process named Synchronized Tool and Roller (STR) diamond machining is developed in NUS & SIMTech joint project [16] to solve the problem illustrated above which is currently faced by the industry. A four- axis synchronized tool–workpiece interactive motion is designed to realize precise machining of the radial Fresnel lens microstructures containing steep circular grooves on the outer cylindrical surface. The tool path generation algorithm has been developed from geometrical modelling considering the lens design, the tool geometries and the roller parameters.

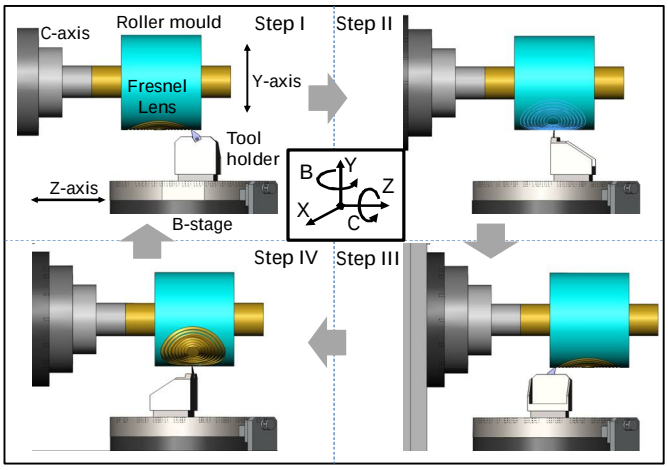

Figure. 16: 4-Axis Integrated Tool-Workpiece Motion[16]

The potential of the STR diamond machining process has been demonstrated by direct machining of a radial Fresnel lens structure with 10 mm diameter and 8.25 nm surface roughness on a roller mould in 8 h, which satisfies the industry requirement of high-precision optical roller moulds.[16]

3.2.2. Development of Free form Surface Patterning technique

The existing methods for FTS diamond turning to fabricate freeform surfaces is non-uniform rational basis spline (NURBS) based freeform machining. This method utilizes the pre-calculated movement table derived from established equations [17]. From the traditional NURBS method to fabricate surface features, have some limitations. Firstly, the process to convert the desired freeform feature into mathematical equations is a complex and challenging task that is not mastered by any layman; moreover, irregular features like hand-drawn features are hard to be defined into mathematical equations. Hence, in order to tackle the limitations mentioned, in NUS a novel process has been developed [18]in that process feature can be directly converted into the machine code (CNC code) for fabrication using FTS diamond Turing. The process for the proposed method is summarized in four main steps:

a. Import the image via MATLAB and convert it into grayscale matrix. Thus to obtain the data information, represented by a two dimensional matrix.
b. Project the gridded matrix onto an estimated Archimedes spiral trajectory.
c. Extract the height of feature from the color information stored in the matrix.
d. Simulate the 3D freeform feature and convert to machine code for fabrication using FTS diamond turning.

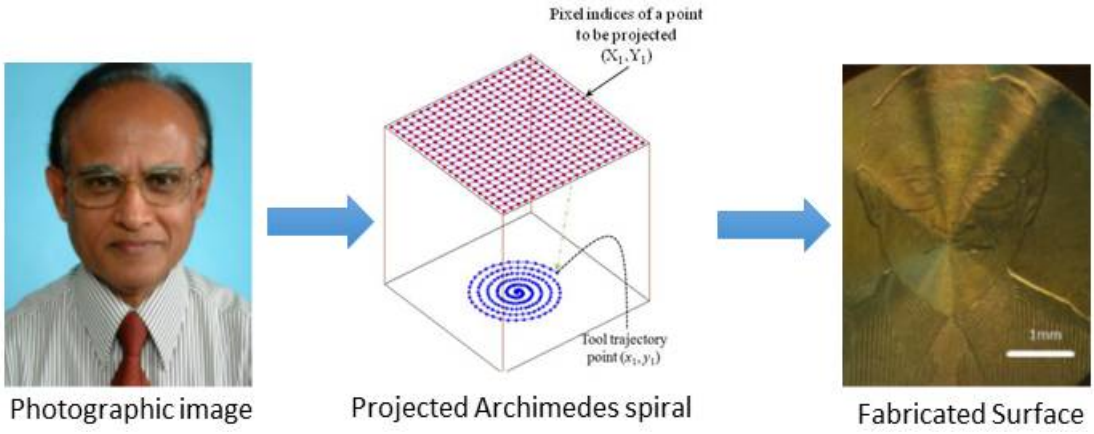

Figure 17: Machining surface with digital image[18]

The proposed methodology has been experimentally validated by the successful machining of freeform features based on any digital image. This process allows even a layman to customize a feature without working out any mathematical equations.

4. Ductile mode Machining of Brittle Materials

If a manufacturing engineer is asked to machine glass which a brittle material in ductile mode he will also argue that it is impossible. However, Nano-indentation results proved that every practical material, no matter how brittle it is, has some plasticity[19]. So, if he is given some clues explaining the fundamental properties of brittle materials that every brittle material has a ductile layer on it as shown in Fig.18 [19], he will be able to unravel the challenge and be easily able to machine brittle materials in ductile mode. In this area in NUS research is mostly focused on the Ductile Mode Machining of Brittle Materials by Micro-End Milling.

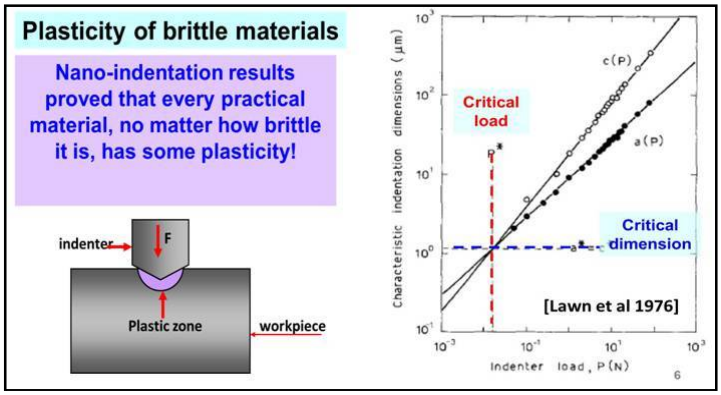

Figure 18: Nano-indentation results of the Plasticity of brittle materials[19]

4.1. Ductile Mode Machining of Brittle Materials by Micro-End Milling

Perhaps, the most significant advantage of micro or nano-scale machining has been realized in machining of brittle materials. Brittle materials such as glass and ceramics are considered as difficult-to-machine materials because of their high tendency towards brittle fracture during machining. The most important challenge in machining these brittle materials is to achieve the material removal by plastic deformation rather than characteristic brittle fracture. Ductile-mode machining is a promising technology to achieve crack-free machined surfaces on brittle materials. Ductile-mode machining is mostly performed by single edge cutting process which is usually diamond turning. However diamond turning has limited capability to machine three dimensional shapes and asymmetrical features on work-material. Micro-endmilling is a versatile machining process capable of machining complex shapes, cavities, asymmetrical profiles and prismatic surfaces on work material. In NUS comprehensive research on Ductile Mode Machining of Brittle Materials by micro-end milling machining process is conducted[20, 21] to understand the underlying mechanism of material removal in end milling of brittle materials and influence of machining parameters on the machining mechanism have been investigated both analytically and experimentally. Experimental results have established that fracture-free slots can be machined in glass by micromilling process within the controlled set of cutting conditions.The analytical work was focused on the determination and prediction of critical conditions for ductile-brittle transition in milling process of brittle material in terms of process parameters such as unreformed chip thickness and feed per edge. The feed per edge and the axial depth of the cut have been identified as the critical factors for the ductile–brittle transition in micro cutting of glass by milling process. Three modes of machining achieved as shown in Fig 19.

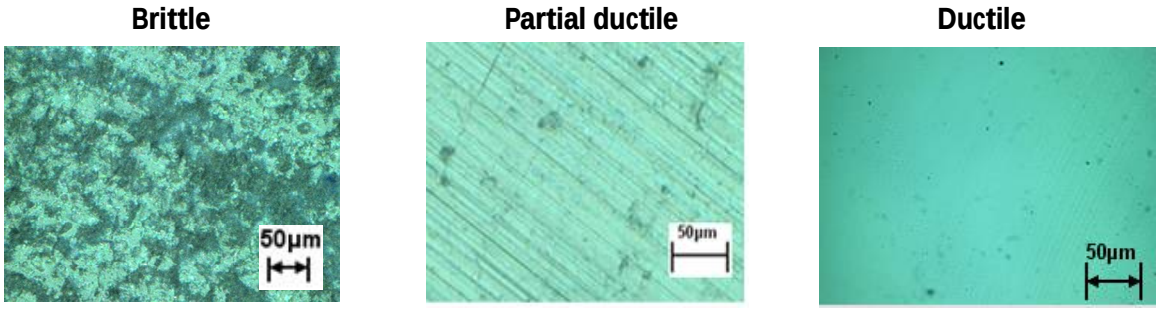

Radial depth of cut= 150µm, feed rate=6 mm/min

Radial depth of cut=350µm, feed rate= 4.0 mm/min

Radial depth of cut=275 µm, feed rate= 4 mm/min

Figure 19: Three Modes of Machining Achieved-a Typical example of transition of machining modes from brittle to ductile depending on cutting conditions on Silicon. (Machine used: DT-110)

(The cutting speed was constant = 9.42 m/min during all experimental conditions. The feed per edge for brittle mode =1.5 micron, for partial mode = 1 micron, ductile = 1 micron. The critical chip thickness for all cases is ~0.3 micron. The first brittle point occurs at about 28 degree angle in upmilling cut.)

5. Conclusion

A multi-purpose miniature machine tool has been developed for high precision micro machining in NUS. The machine is capable of performing micro-EDM, micro-ECM, micro-WEDG, micro-turning and micro-milling. Special process developed for the machine included the fabrication a high-aspect-ratio micro-structure using micro-EDM. This is possible through fabrication of a very fine electrode on-machine by sacrificial electrodes or micro-turning, and then micro-EDM is performed to fabricate a micro-structure using the electrode. A series of micro features have been successfully fabricated using the technique developed. A desktop ultra precision lathe incorporating a high speed spindle and fast/fine tool servo system has also been developed in order to achieve economical nano surface generation by diamond turning. Attempt to develop a novel image patterning process, and Synchronized Tool and Roller (STR) diamond machining process have been successful. Developed Synchronized Tool and Roller (STR) diamond machining process is capable of direct machining of a radial Fresnel lens structure on roller moulds. All of these research is expected to make significant contribution towards miniaturization.

References:

1. Okuyama, H. and H. Takada, *Micromachining with SR and FEL*. Nuclear Instruments and Methods in Physics Research Section B: Beam Interactions with Materials and Atoms, 1998. **144**(1–4): p. 58-65.
2. Rajurkar, K.P. and Z.Y. Yu, *3D Micro-EDM Using CAD/CAM.* CIRP Annals - Manufacturing Technology, 2000. **49**(1): p. 127-130.
3. Asad, A.B.M.A., *Micro-EDM Process for Tool-based Compound Micromachining.* Ph.D. Thesis, National University of Singapore, 2012.
4. Azizur Rahman, M., et al., *CNC microturning: an application to miniaturization.* International Journal of Machine Tools and Manufacture, 2005. **45**(6): p. 631-639.
5. Rajurkar, K.P., et al., *Micro and Nano Machining by Electro-Physical and Chemical Processes.* CIRP Annals - Manufacturing Technology, 2006. **55**(2): p. 643-666.
6. Lauwers, B., *Surface Integrity in Hybrid Machining Processes.* Procedia Engineering, 2011. **19**: p. 241-251.
7. Rahman, M., et al., *A multiprocess machine tool for compound micromachining.* International Journal of Machine Tools and Manufacture, 2010. **50**(4): p. 344-356.
8. Rahman, M., Y.S. Wong, and M.D. Nguyen, *11.06 - Compound and Hybrid Micromachining: Part II – Hybrid Micro-EDM and Micro-ECM*, in *Comprehensive Materials Processing*, S.H.F.B.J.V.T. Yilbas, Editor. 2014, Elsevier: Oxford. p. 113-150.
9. Mikrotools, *http://mikrotools.com/*. 2015.
10. Asad, A.B.M.A., et al., *Tool-based micro-machining.* Journal of Materials Processing Technology, 2007. **192–193**: p. 204-211.
11. Lim, H.S., A.S. Kumar, and M. Rahman, *Improvement of form accuracy in hybrid machining of microstructures.* Journal of Electronic Materials, 2002. **31**(10): p. 1032-1038.
12. Nguyen, M.D., M. Rahman, and Y.S. Wong, *Simultaneous micro-EDM and micro-ECM in low-resistivity deionized water.* International Journal of Machine Tools and Manufacture, 2012. **54–55**: p. 55-65.
13. Rahman, M., et al. *Compound Micro/Nano Machining–A Tool-Based Innovative and Integrated Approach*. in *Key Engineering Materials*. 2010. Trans Tech Publ.
14. Hansen, H.N., R.J. Hocken, and G. Tosello, *Replication of micro and nano surface geometries.* CIRP Annals - Manufacturing Technology, 2011. **60**(2): p. 695-714.
15. Linfa, P., et al., *Micro hot embossing of thermoplastic polymers: a review.* Journal of Micromechanics and Microengineering, 2014. **24**(1): p. 013001.
16. Huang, R., et al., *Ultra-precision machining of radial Fresnel lens on roller moulds.* CIRP Annals - Manufacturing Technology, 2015. **64**(1): p. 121-124.
17. Brecher, C., et al., *NURBS Based Ultra-Precision Free-Form Machining.* CIRP Annals - Manufacturing Technology, 2006. **55**(1): p. 547-550.
18. Neo, W.K., et al., *Novel Machining Technique for Surface Patterning by Diamond Turning.*
19. Lawn, B.R., T. Jensen, and A. Arora, *Brittleness as an indentation size effect.* Journal of Materials Science, 1976. **11**(3): p. 573-575.
20. Arif, M., M. Rahman, and W.Y. San, *Ultraprecision ductile mode machining of glass by micromilling process.* Journal of Manufacturing Processes, 2011. **13**(1): p. 50-59.
21. Arif, M., et al., *An experimental approach to study the capability of end-milling for microcutting of glass.* The International Journal of Advanced Manufacturing Technology, 2011. **53**(9-12): p. 1063-1073.

International Conference on Mechanical, Industrial and Materials Engineering 2015 (ICMIME2015)
11-13 December, 2015, RUET, Rajshahi, Bangladesh.

Paper ID: KL-03

Aerodynamics of Multiple Structures: Wake and Flow-Induced Force

Md. Mahbub Alam

Institute for Turbulence-Noise-Vibration Interaction and Control, Shenzhen Graduate School, Harbin Institute of Technology, Shenzhen Graduate School, Shenzhen, China
E-mail: alamm28@yahoo.com; alam@hitsz.edu.cn

Abstract

Multiple cylindrical structures subjected to fluid flow are rife in engineering, e.g., tube bundles in heat exchangers, cables of cable-stayed bridges, overhead power-line bundles, chemical reaction towers, offshore structures, pipelines under the sea, chimney stacks, pin fins used for cooling turbine blade or electronic equipments, and skyscrapers in modern cities. Failure of these structures results from fluid-structure-interaction-generated fluctuating fluid forces, structural vibrations, acoustic noise, or resonance. The knowledge of fluid-structure interactions is thus very crucial for the designer to provide a longer life to the structures. Here physics of flow around two tandem circular cylinders of identical diameter is studied numerically at Reynolds number Re = 200 using finite volume discretization. The spacing ratio L^* = L/D is varied from 2 to 9, where L is the cylinder center-to-center spacing and D is the cylinder diameter. We focus on fluctuating (rms) lift coefficient C_{Lf} of the upstream cylinder and phase lag ϕ between vortex sheddings from the two cylinders for L^* larger than the critical where the co-shedding flow prevails. As known before, ϕ is a linear function of L^*, but it is, as proved presently, indeed a nonlinear function of L^*. The ϕ turns out to be inphase and antiphase alternately as L^* increases. We unearth that the upstream cylinder C_{Lf} is affected by both L^* and ϕ. While the contribution of L^* to C_{Lf} diminishes rapidly with L^* in an overdamped manner, that of ϕ makes the L^*-dependent C_{Lf} variation underdamped sinusoidal, persisting in the L^* range examined. The inphase and antiphase flows respectively correspond to a local maximum and minimum C_{Lf}, respectively.

Keywords: cylinders, tandem, phase lag, pressure, flow, wake.

1. Introduction

Flow interference between the cylinders is non-linear and very complex as Reynolds number (*Re*, based on the cylinder diameter *D* and the free-stream velocity U_∞) and spacing ratio L^* (= *L/D*, where *L* is the cylinder center-to-center spacing) are changed. Zdravkovich [1] identified three flow regimes for two tandem cylinders: extended-body/overshoot regime (L^* < 1.2 - 1.8, depending on *Re*), reattachment regime (1.2 - 1.8 < L^* < 3.4 - 3.8), and co-shedding regime (L^* > 3.4 - 4.0). Alam *et al*. [2] further divided the reattachment regime into alternating reattachment (1.5 < $L^* \leq$ 3.0) and steady reattachment (3.0 < $L^* \leq$ 4.0) regimes. The boundaries of the different regimes are highly dependent on *Re* [3]. The spacing differentiating the second and third regimes is known as critical spacing L_c^*. There have been very few scattered studies in which fluctuating (rms) lift C_{Lf} and fluctuating drag C_{Df} are measured. Detailed measurements of C_{Lf} and C_{Df} including time-mean drag C_D, Strouahl number *St*, and time-mean and fluctuating pressures at $Re = 6.5\times10^4$ were done by Alam *et al*. [2].

Alam *et al*. [4] pioneered that ϕ has a significant effect on C_{Lf} of the upstream cylinder, local maxima and minima of C_{Lf} corresponding to two cylinders' vortex sheddings occurring at and antiphase, respectively. They provided an explanation that when two cylinders are at inphase mode, the shear layer of the downstream cylinder accelerates the same-side shear layer of the upstream cylinder. Similarly, in the next half cycle, the other side shear layer is also accelerated. The C_{Lf} of the upstream cylinder is thus enhanced, showing local maximum at inphase mode. On the other hand, when two cylinders are at antiphase mode, the shear layer of the downstream cylinder accelerates the same-side shear layer of the upstream cylinder in which the action of the shear layer that sheds from the opposite side of the upstream cylinder is reduced; thus the condition corresponds to a minimum C_{Lf}. Between these two extremities, the action changes gradually so that C_{Lf} variation with L^* follows a sine curve with decreasing amplitude. Indeed, the explanation was perhaps a best guess without substantiation.

The objective of this work is to find the relationship between ϕ, C_{Lf} and L^* and provide an insightful physics of the relationship. A detailed 2-dimensional numerical simulation is conducted at *Re* = 200. C_{Lf}, *St* and ϕ are

estimated and presented as functions of L^*. Furthermore, to assimilate the insight into the relationship between ϕ, C_{Lf} and L^*, we extracted velocity and pressure fields and information on vortex dynamics.

2. Computation

The governing equations for an unsteady, viscous, laminar and incompressible fluid flow with constant properties are the continuity and momentum equations expressed in Cartesian coordinate as

$$\frac{\partial u}{\partial x}+\frac{\partial v}{\partial x}=0;\ \frac{\partial u}{\partial t}+u\frac{\partial u}{\partial x}+v\frac{\partial u}{\partial y}=-\frac{\partial P}{\partial x}+\frac{1}{\mathrm{Re}}(\frac{\partial^2 u}{\partial x^2}+\frac{\partial^2 u}{\partial y^2}),\ \text{and}\ \frac{\partial v}{\partial t}+u\frac{\partial v}{\partial x}+v\frac{\partial v}{\partial y}=-\frac{\partial P}{\partial x}+\frac{1}{\mathrm{Re}}(\frac{\partial^2 v}{\partial x^2}+\frac{\partial^2 v}{\partial y^2}),$$

where u and v are the velocity components in the x and y directions, respectively, P is the pressure and t is the time. The three differential equations are coupled and solved for the unknown P, u and v. The computations are performed using Ansys-Fluent solver based on the finite volume method. While a standard scheme and a second-order upwind scheme are used to discretize pressure and velocity, respectively, the first-order implicit formulation is used for time discretization. The coupling between the pressure and velocity fields is achieved using the SIMPLE technique.

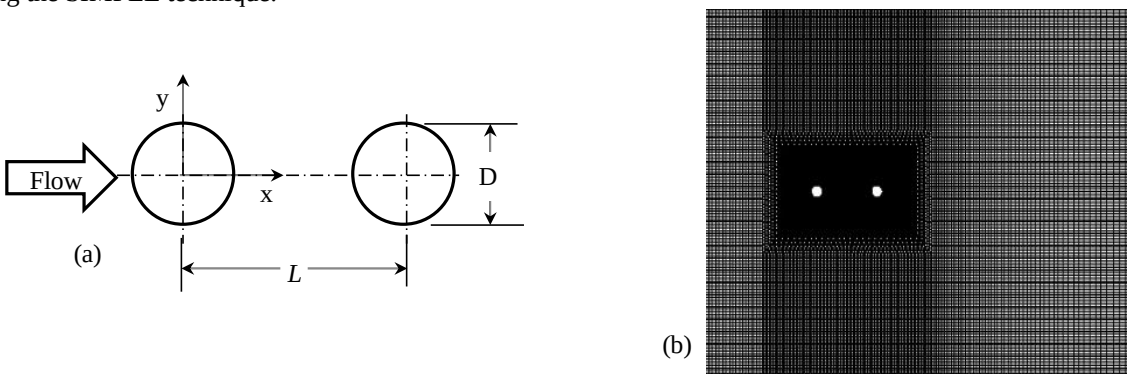

Fig. 1. (a) Cylinder arrangement and definitions of symbols, and (b) typical grid structure.

The two cylinders have the same diameter D, and the spacing between their centers is L. The schematic diagram of the flow model is given in Fig. 1(a). The computational domain was 65D in the streamwise direction and 30D in the cross-stream direction, which gives a blockage ratio of 3.3% only. The cylinder diameter and freestream velocity were 20 mm and 0.146 m/s, respectively, corresponding to Re = 200. The inlet boundary was 15D away from the center of the upstream cylinder. An O-xy grid system near the cylinders and a rectangular grid system away from the cylinders were used as shown in Fig. 1(b). The grid system was generated using Gambit. The number of grids for the O-grid system was 200 in the transverse direction and 60 in the radial direction. Therefore, a total of 200 points were on the cylinder surface. The grid in the radial direction was denser near the cylinder surface with the nearest grid being 0.005D away from the cylinder surface. While the no-slip boundary conditions are employed on the surfaces of the cylinders, the free-slip boundary condition is adopted for the upper and lower boundary walls. That is, $u = v = 0$ on the surfaces of the cylinders; $u = U_\infty$, and $v = 0$ at the lower and upper walls; $u = U_\infty$, and $v = 0$ at the inlet; and $\partial u/\partial x = 0$ and $\partial v/\partial x = 0$ at the outlet.

3. Grid Independence Test and Result Validation

Five different meshes (nodes 33000, 38000, 56000, 66700, 89000) for a single cylinder are checked with a time step varied as 0.05, 0.01 and 0.005 sec. The forces and St results converged for nodes 38000 and time step 0.01 sec that yielded a Courant number less than 0.2 in the whole domain. Table 1 compares C_D, C_{Lf} and St results obtained by us and others. Present data display a good accord with the data by others. The departure of the present results from those in the other literature is less than 4%, 3%, and 3% for C_D, C_{Lf} and St, respectively.

Table 1. Comparison of C_D, C_{Lf} and St for a single cylinder at Re = 200.

	C_D	C_{Lf}	St
Present, CFD	1.4	0.488	0.195
[5], CFD	1.43	0.496	0.196
[6], CFD	1.37	0.502	0.196
[7], CFD	1.38	0.495	0.192
[8], CFD	1.37	0.495	0.190
[9], exp	--	--	0.196

4. Relationship between C_{Lf} and ϕ

A concurrent plot of ϕ and C_{Lf} of the upstream cylinder with change in L^* is presented in Fig. 2(a). C_{Lf} firstly wanes rapidly (up to $L^* \approx 5.25$) and then grows before declining again from $L^* \approx 7.5$. Given that, at $L^* = L_c{}^*$, ϕ is approximately 2π, irrespective of bluff body shape. Here ϕ at $L^* = 3.65$ is slightly higher than 2π, since $L_c{}^*$ is not exactly at 3.65 but smaller, between 3.5 and 3.65, as mentioned before. C_{Lf} variation shows local maxima at $L^* =$ 3.65 and 7.5 and a local minimum at $L^* \approx 5.25$. The former two L^* correspond to $\phi \approx 2\pi$ and 4π, respectively, inphase shedding (Fig. 2b, d). On the other hand, the latter corresponds to $\phi = 3\pi$, antiphase shedding (Fig. 2c). That is, it can generally be said that the local maximum and minimum of C_{Lf} occur when $\phi = 2n\pi$ and $(2n+1)\pi$, respectively (where n = 1, 2, 3 …). The C_{Lf} variation with L^* is very similar to a damped oscillation with the magnitude of the local maximum or minimum diminishing with L^*, insinuating that the C_{Lf} variation with L^* is composed of two, one associated with L^* only and the other associated with ϕ that is also function of L^* which will be discussed later after assimilating how ϕ influences the flow around the upstream cylinder.

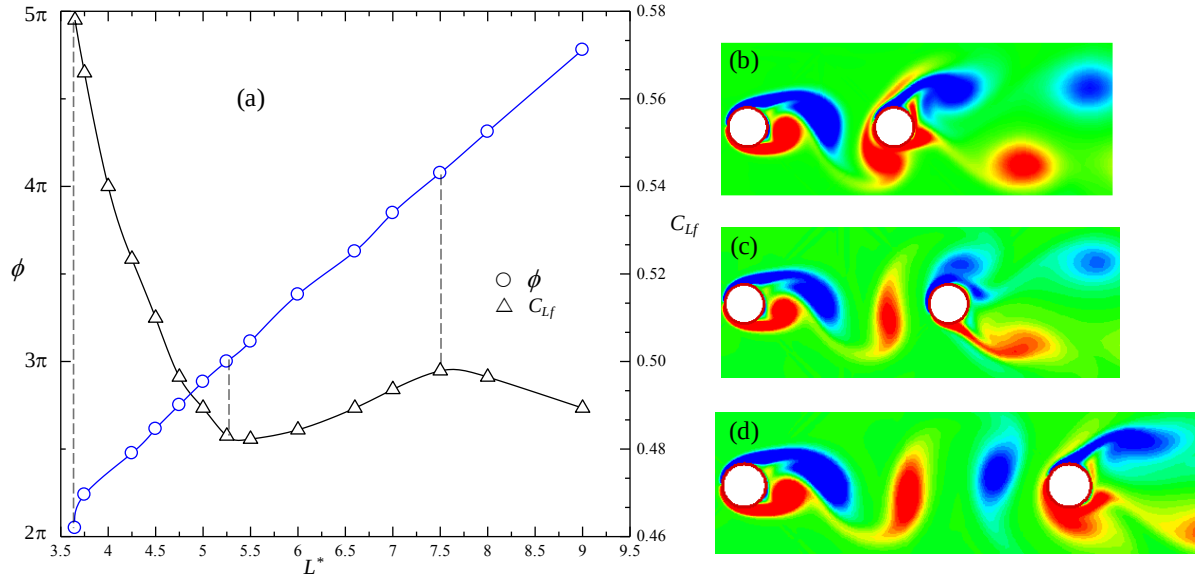

Fig. 2. (a) Relationship between ϕ, L^* and C_{Lf} of the upstream cylinder ($L^* > 3.65$) and (b, c, and d) vorticity patterns at $L^* =$ 3.65, 5.25 and 7.5, respectively.

5. Dependence of Flow structure on L^*

L^* affects the mean parameters to a great extent. Contours of normalized time-mean streamwise velocity $\bar{u}^*$ ($= \bar{u}/U_\infty$, where $\bar{u}$ is the local time-mean streamwise velocity) around the upstream and downstream cylinders are shown in Fig. 3 at $L^* =$ 3.65, 4.25, 5.25, 6.5, and 7.5. The region enclosed by $\bar{u}^* = 0$ is known as the recirculation region or wake bubble. With increase in L^*, (i) the wake bubble size of either cylinder enlarges particularly in the streamwise direction, the extent is however greater for the downstream cylinder, (ii) the velocity gradient $\partial\bar{u}^*/\partial x^*$ behind the upstream cylinder along the wake centerline $y^* = 0$ becomes greater in the domain $\bar{u}^* > 0$, and (iii) the negative velocity in the wake bubble of either cylinder is enhanced [10]. All these observations imply that a larger L^* enables a greater the flow from the freestream sides into the wake behind the upstream cylinder. While the shear layer thickness (say, lateral width from the cylinder surface to maximum velocity) of the upstream cylinder is narrow, that of the downstream cylinder is very wide. The narrow shear layer is also reflected from more densely arranged contours near the separation for the upstream cylinder than the other. Another interesting feature is that the maximum streamwise velocity $\bar{u}^*_{max}$ in the upper or lower side augments when L^* is increased. To make the observation more clear, $\bar{u}^*_{max}$ is plotted in figure 3(f).

Minimum velocity $\bar{u}^*_{\min}$ in the recirculation bubble behind the downstream cylinder displays an exponential decrease with L^* (figure 3g) with an interruption at $L^* =$ 5.25. The decrease in $\bar{u}^*_{\min}$ with L^* results from the gradually enhanced flow between the cylinders.

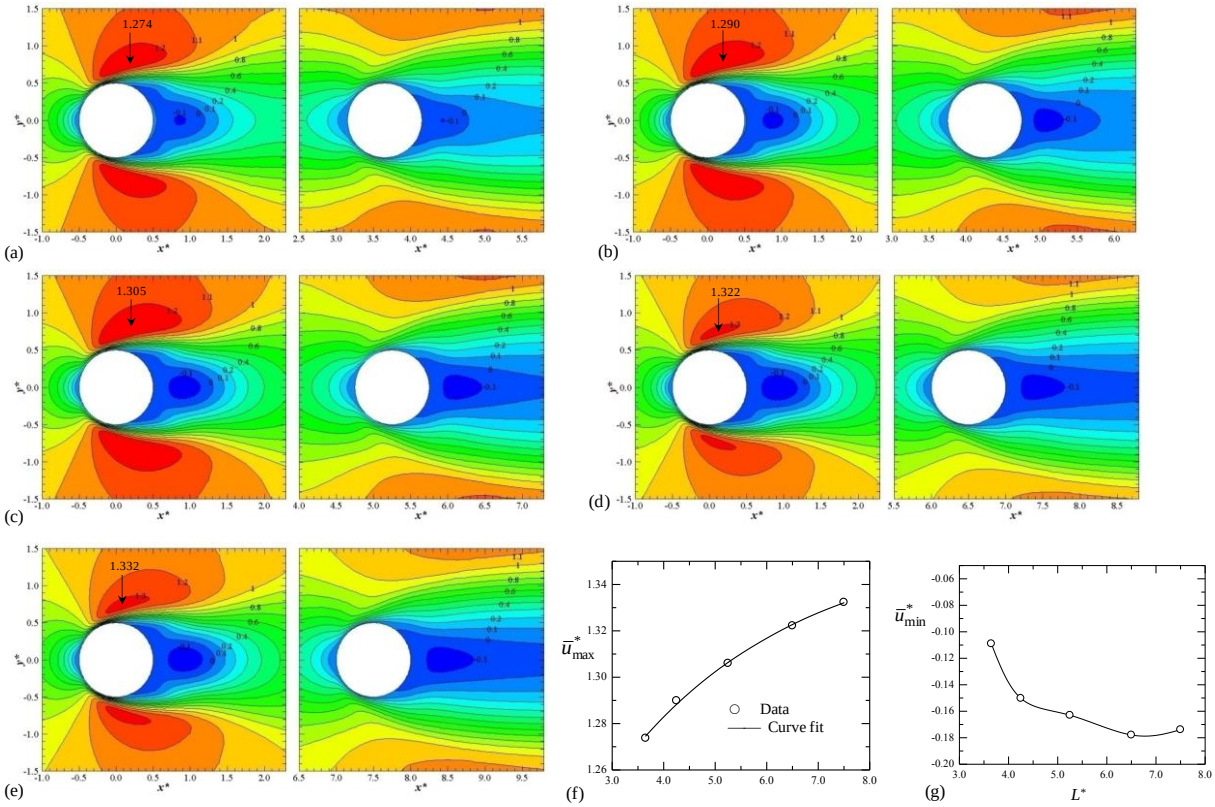

Fig. 3. Contours of time-mean streamwise velocity $\bar{u}^*$ around the upstream and downstream cylinders at (a) L^* = 3.65, (b) 4.25, (c) 5.25, (d) 6.5, and (e) 7.5. (f) Maximum time-average streamwise velocity $\bar{u}^*_{max}$, extracted from (a - e), on the upper or lower side of the upstream cylinder. (g) Minimum velocity $\bar{u}^*_{\min}$ in the recirculation bubble behind the downstream cylinder, extracted from (a - e).

6. Dependence of Coherent Flow on L^*

In order to obtain a clearer understanding of the coherent flow, contours of fluctuating (rms) pressure C_{Pf} around the upstream and downstream cylinders are presented in Fig. 4(a - e) for L^* = 3.65, 4.25, 5.25, 6.5 and 7.5, where L^* = 3.65, 4.25, and 5.25 correspond to C_{Lf} decreasing from a maximum to minimum and L^* = 5.25, 6.5 and 7.5 correspond to C_{Lf} increasing from a minimum to maximum. When L^* increases from 3.65 to 5.25 (i.e., when the flow structure changes from inphase to antiphase), C_{Pf} on the upper and lower sides of the upstream cylinder weakens rapidly. On the other hand, as L^* changes from 5.25 to 7.5 (i.e, when the flow structure transmutes from antiphase to inphase), C_{Pf} on both sides rises albeit slowly. A higher value is found for inphase condition L^* = 3.65 and 7.5, while a relatively small value for antiphase condition L^* = 5.25. In order to comprehend the trend more conspicuously, maximum fluctuating pressure $C_{Pf,max}$ on the upstream cylinder surface is plotted as in Fig. 4(f). Now the difference is obvious, $C_{Pf,max}$ waning at 3.65 < L^* < 5.25 and boosting at 5.25 < L^* < 7.5. The change is smaller at larger L^*, consistent with the variation in C_{Lf}. The overall trend is similar to that of C_{Lf}. It is worthwhile to point out that the recovery of $C_{Pf,max}$ between L^* = 5.25 and 7.5 is not the same as much as $C_{Pf,max}$ loses between L^* = 3.65 and 5.25. That is, though the flow is inphase at both L^* = 3.65 and 7.5, $C_{Pf,max}$ is not the same at the two L^*. The deficit is obviously connected to the effect of L^*.

7. Effect of ϕ on the Coherent Flow

Since L^* mainly influences the mean flow field, the effect of ϕ on the flow field or a parameter can be understood from the instantaneous fluctuating field that can be obtained as the instantaneous field minus mean field, for instance, instantaneous fluctuating pressure coefficient $\tilde{C}_P = C_P - \overline{C_P}$, where C_P is the instantaneous pressure coefficient and $\overline{C_P}$ is the time-mean pressure coefficient. In other words, $\tilde{C}_P$ is the pressure where the datum is the mean pressure.

Indeed, during Karman vortex shedding from a cylinder, the difference between the flow on the upper and lower sides is the largest when C_L is maximum or minimum. Since our focus is to understand how ϕ influences the

flow on the upper and lower sides of the upstream cylinder, $\tilde{C}_P$ at instant corresponding to the minimum C_L of the upstream cylinder will be compared at different L^*. Figure 5(a-e) illustrates $\tilde{C}_P$ field at different L^* where the C_P field corresponds to the minimum C_L (solid circle) as presented in the C_L histories at the top of each L^*. At the top, the solid and dashed lines denote the lift histories of the upstream and downstream cylinders, respectively. $\tilde{C}_P$ for the upstream cylinder is positive on the upper side and negative on the lower side, which indicates the shedding happening on the lower side of the upstream cylinder. The shedding (negative pressure on the lower surface) from the downstream cylinder occurs from the lower side at L^* =3.65 (inphase), upper side at L^* = 5.25 (antiphase) and lower side at L^* = 7.5 (inphase). It is obvious that $\tilde{C}_P$ magnitude on either side of the upstream cylinder dwindles for L^* = 3.65 - 5.25 where ϕ transforms from inphase to antiphase and escalates for L^* = 5.25 - 7.5 where ϕ modifies from antiphase to inphase; the $\tilde{C}_P$ trend resembles C_{Lf}. A more fragrant topography can be viewed from a plot of maximum and minimum $\tilde{C}_P$ (i.e., $\tilde{C}_{P,\max}$, $\tilde{C}_{P,\min}$) as a function of L^* (Fig. 5f). In the range L^* = 3.65 - 5.25, $\tilde{C}_{P,\max}$ and $\tilde{C}_{P,\min}$ wane and augment, respectively, indicating that the flow over the upper side of the upstream cylinder accelerates with L^* and that over the lower side decelerates, when ϕ transforms from inphase to antiphase. The opposite phenomenon prevails at L^* = 5.25 - 7.5.

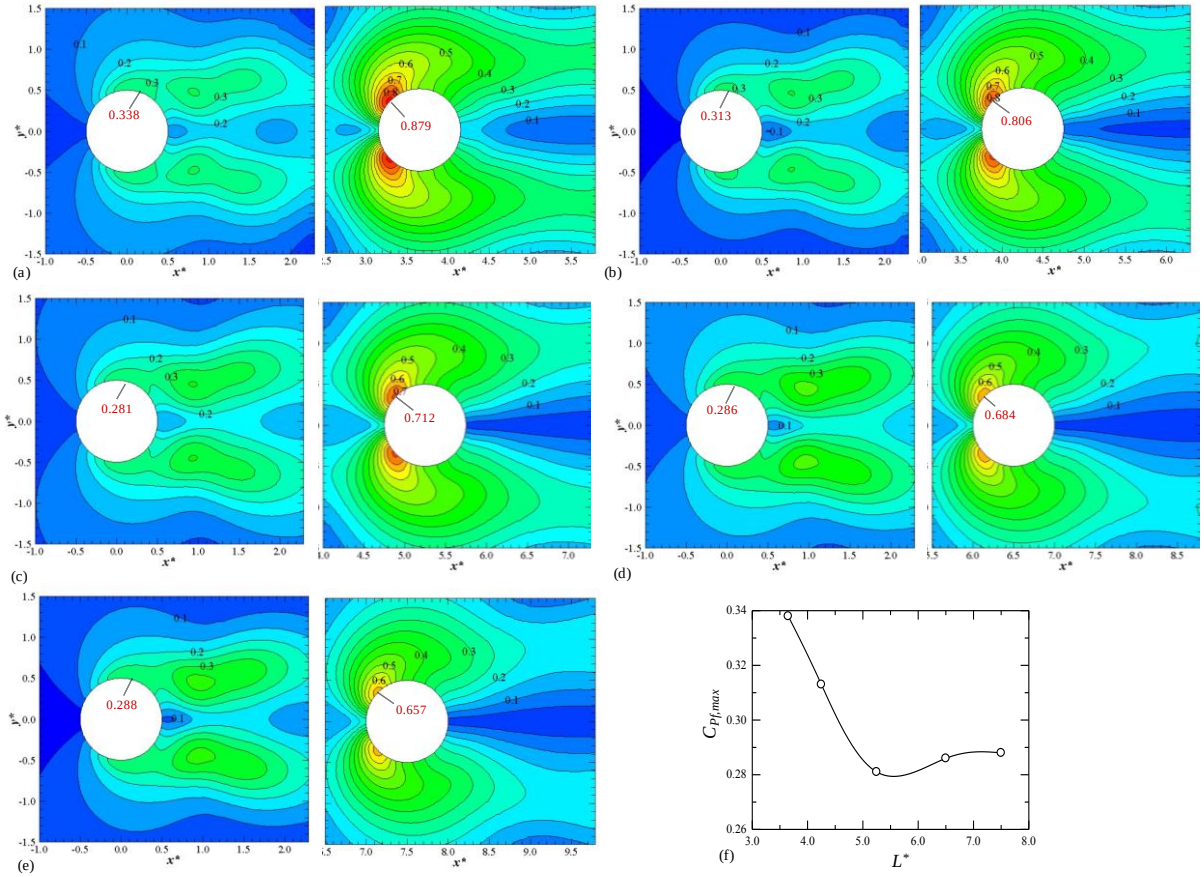

Fig. 4. Contours of fluctuating (rms) pressure coefficient C_{Pf} at (a) L^* = 3.65, (b) 4.25, (c) 5.25, (d) 6.5, and (e) 7.5. (f) Variation in maximum fluctuating pressure coefficient $C_{Pf,max}$ on the upstream cylinder with L^*.

The remark is again reflected in $\tilde{u}^* = u^* - \bar{u}^*$ field in Fig. 6, where $\tilde{u}^*$ is presented around the upstream cylinder only. Negative and positive $\tilde{u}^*$ on the upper and lower sides, respectively, are the signatures of smaller u^* on the upper side and higher u^* on the lower side, consistent with positive and negative $\tilde{C}_P$, respectively. Once more, $\tilde{u}^*_{\max}$ and $\tilde{u}^*_{\min}$ displayed in Fig. 6(f) reflect the same view, velocity increasing on the upper surface and decreasing on the lower surface when ϕ changes from inphase to antiphase at L^* = 3.65 - 5.25, and vice versa at L^* = 5.25 - 7.5. Now it is clear that the effect of ϕ is dependent on L^* as well, feeble at a larger L^*. Similarly, instantaneous fluctuating cross-stream velocity $\tilde{v}^* = v^* - \bar{v}^*$ is presented in Fig. 7(a-e). Two peaks are observed along the wake centerline at $x^* \approx 1.5$ and 2.6, respectively. The first peak is positive, caused by the

shedding from the lower side. On the contrary, the second peak is negative, attributed to a separated vortex from the upper side. A small peak at the base of the cylinder is induced by the anticlockwise rolling of the vortex from the lower side. $\tilde{v}^*$ values at the two dominant peaks ($\tilde{v}^*_{\max}$ and $\tilde{v}^*_{\min}$) are plotted in Fig. 7(f) as a function of L^*. $\tilde{v}^*_{\max}$ recovers at L^* = 5.25 - 7.5 where $\tilde{u}^*_{\max}$ does the same. When velocity in the upper shear layer increases between L^* = 3.65 and 5.25, $\tilde{v}^*$ peak magnitude associated with the shear layer decays, as the growing shear layer on the downstream cylinder tends to pull the downward flow upward. On the contrary, between L^* = 5.25 and 7.5, the growing lower shear layer of the downstream cylinder tends to accelerate the downward flow of the upper shear layer. That is, the inphase shedding can bring more fluid from freestream into the gap between the cylinders than the antiphase.

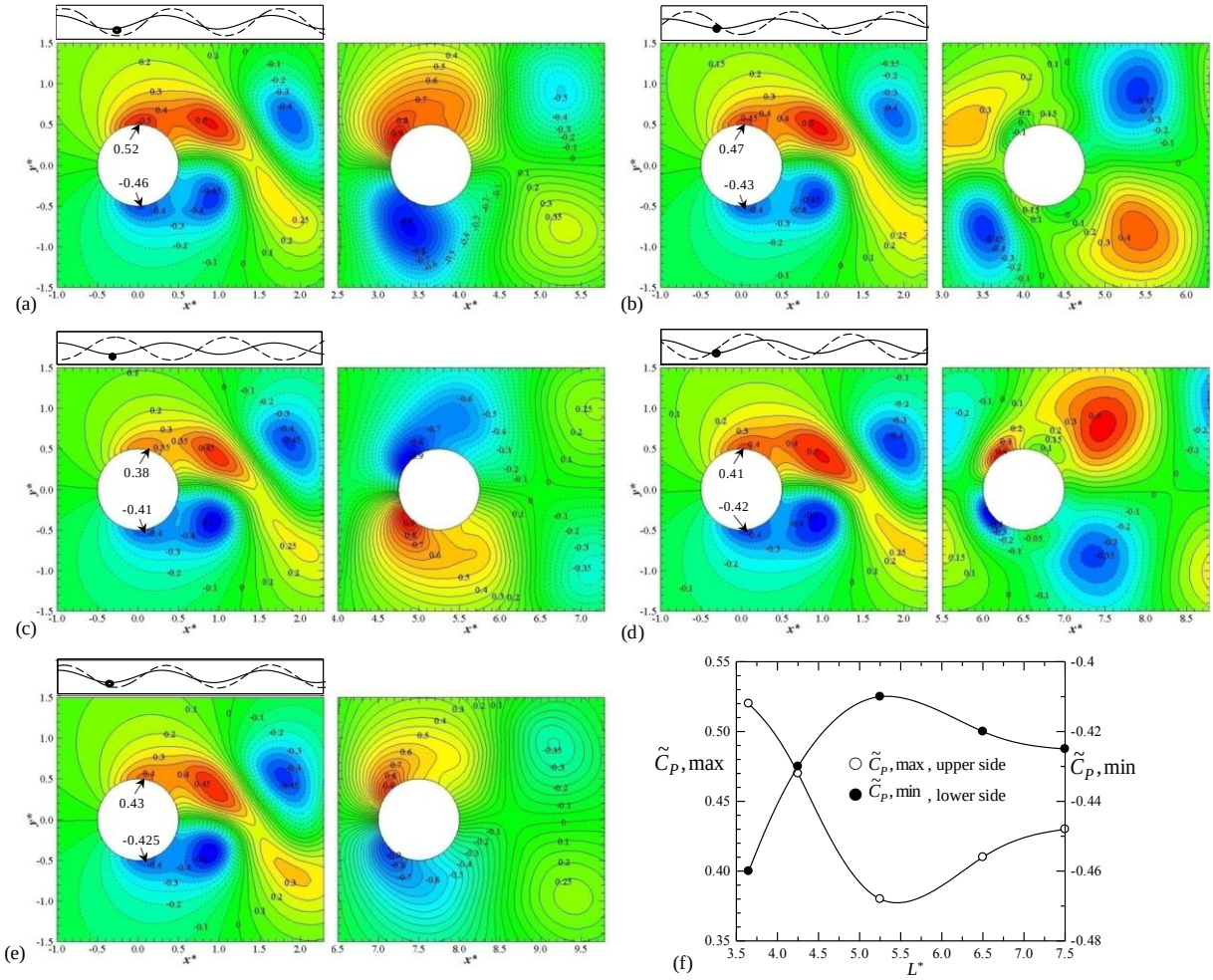

Fig. 5. Contours of $\tilde{C}_P = C_P - \overline{C_P}$ around the two cylinders when the upstream cylinder is subjected to the minimum lift (downward) at (a) L^* = 3.65, (b) 4.25, (c) 5.25, (d) 6.5, and (e) 7.5. (f) Dependences on L^* of maximum and minimum $\tilde{C}_P$ (i.e., $\tilde{C}_{P,\max}$ and $\tilde{C}_{P,\min}$) on the upper and lower sides of the upstream cylinder.

8. Decomposition of the Effect of L^* and ϕ on C_{Lf}

The effect of L^* and ϕ on C_{Lf} can also be extracted from a curve fitting of C_{Lf}.
Based on the above results and discussion, C_{Lf} can be written as,

$$C_{Lf} = Ae^{-\alpha L^*} + \eta \sin(\phi + \frac{\pi}{2}) + C \tag{1a}$$

Even for a given ϕ, the influence of ϕ at different L^* would be different, weaker at a larger L^*. η may, therefore, be again in an exponential form.

Eq. (1a) then can be written as

$$C_{Lf} = Ae^{-\alpha L^*} + Be^{-\beta L^*} \sin(\phi + \frac{\pi}{2}) + C \tag{1b}$$

The constants A, α, B, β and C can be obtained from the C_{Lf} vs L^* curve.

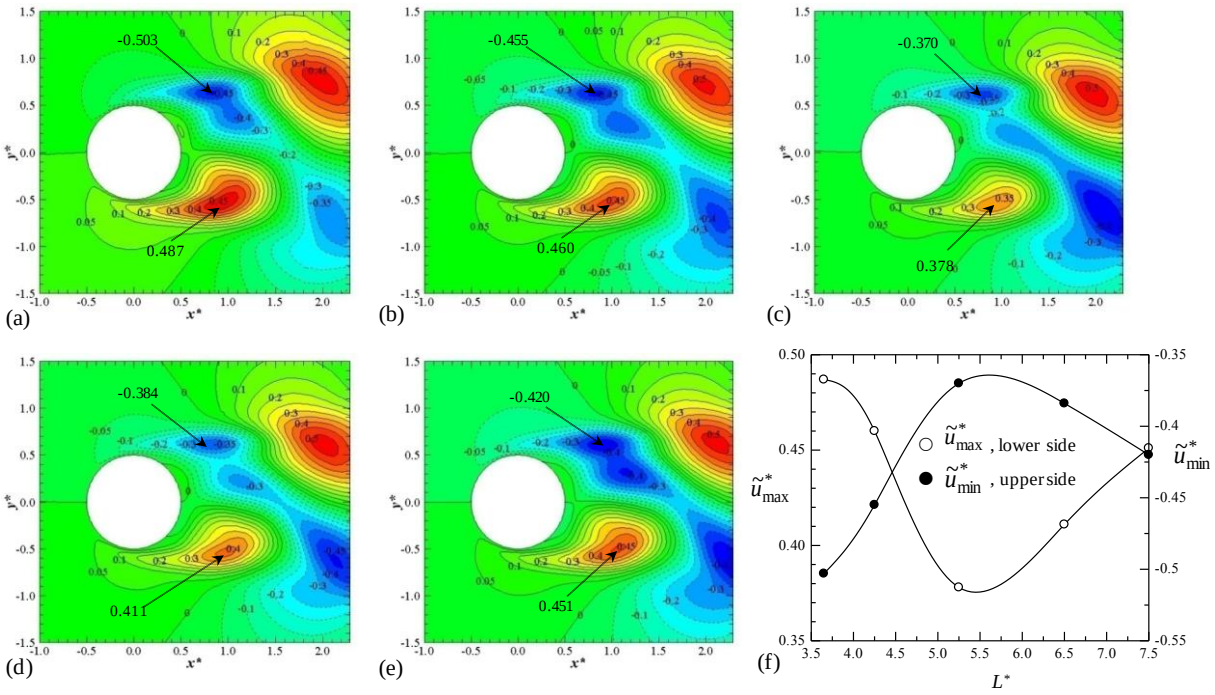

Fig. 6. Contours of $\tilde{u}^* = u^* - \bar{u}^*$ around the upstream cylinder when the upstream cylinder is subjected to the minimum lift (downward) at (a) L^* = 3.65, (b) 4.25, (c) 5.25, (d) 6.5, and (e) 7.5. (f) Dependence on L^* of maximum and minimum $\tilde{u}^*$ (i.e., $\tilde{u}^*_{max}$ and $\tilde{u}^*_{min}$) on the upper and lower sides of the cylinder.

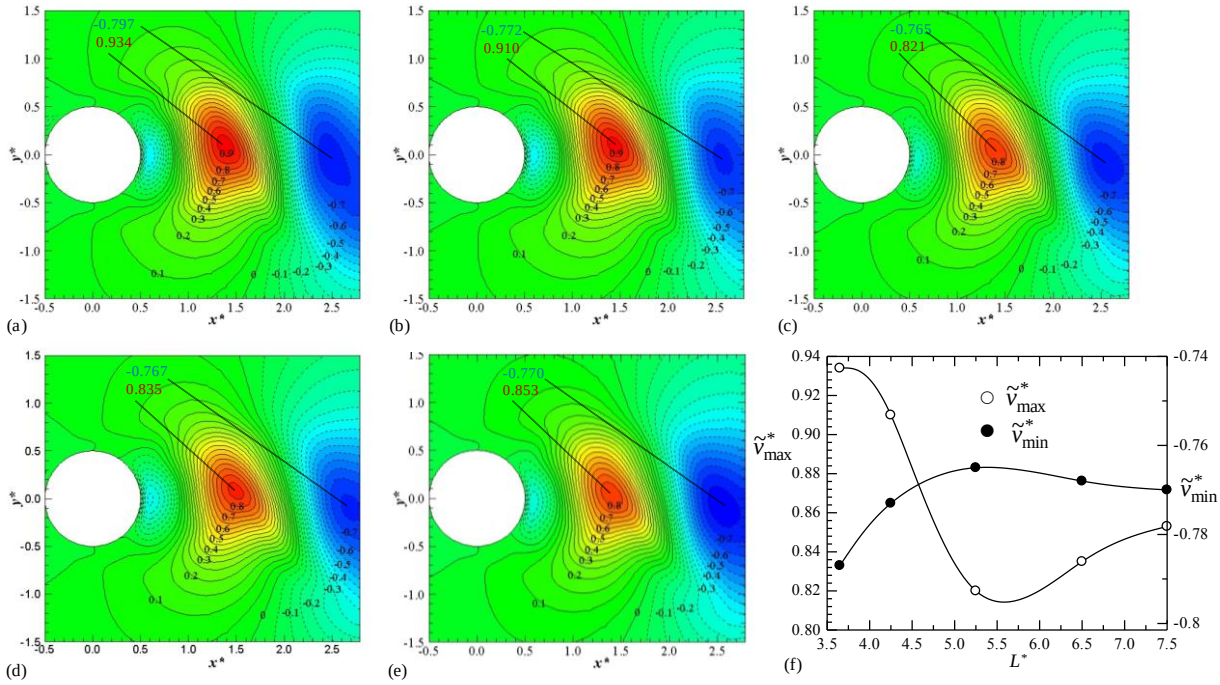

Fig. 7. Contours of $\tilde{v}^* = v^* - \bar{v}^*$ when the upstream cylinder is subjected to the minimum lift (downward) at (a) L^* = 3.65, (b) 4.25, (c) 5.25, (d) 6.5, and (e) 7.5. (f) Variation in maximum and minimum $\tilde{v}^*$ (i.e., $\tilde{v}^*_{max}$ and $\tilde{v}^*_{min}$), extracted from (a - e), in the near wake with increase in L^*.

C_{Lf} data obtained (Fig. 2) are fitted following Eq. (1b) as

$$C_{Lf} = 13.8e^{-1.43L^*} + 0.036e^{-0.2L^*}\sin(\phi + \frac{\pi}{2}) + 0.488 \qquad (2a)$$

Interestingly, the last term is equal to single cylinder $C_{Lf,}$ denoted by C_{Lf0}. The equation will therefore be

$$C_{Lf} - C_{Lf0} = \underbrace{13.8e^{-1.43L^*}}_{L^* \text{ induced } C_{Lf}} + \underbrace{0.036e^{-0.2L^*}\sin(\phi + \frac{\pi}{2})}_{\phi \text{ induced } C_{Lf}} \quad (2b)$$

The equation predicts that $C_{Lf} = C_{Lf0}$ at $L^* = \infty$, consistent with our intuition.

While the first term in the right-hand side is associated with the effect of L^* only, the second term is connected to ϕ, reflecting the influence of ϕ at different L^*. We will, therefore, call the first and second terms in the right-hand side as the contributions of L^* and ϕ, respectively.

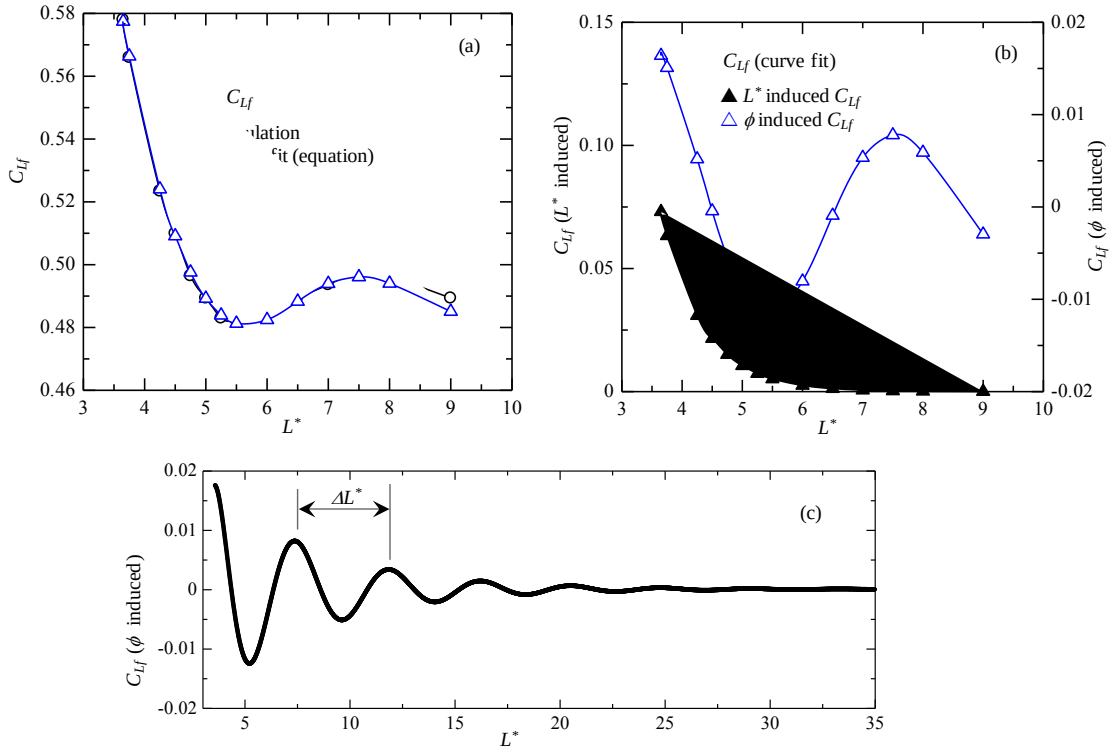

Fig. 8. (a) Upstream cylinder C_{Lf} obtained from simulation and curve fit equation. (b) Decomposed C_{Lf} induced by L^* and ϕ. (c) ϕ induced C_{Lf} from Eq. (2) showing influence of ϕ for a longer range of L^*.

Original and curve fitting (equation) data are presented in Fig. 8(a), showing the closeness between them. In order to get the information on the individual contributions of L^* and ϕ to C_{Lf}, the values of the first and second terms are given in Fig. 8(b). As seen, the contribution of L^* to C_{Lf} declines rapidly, negligible at $L^* > 7.5$, while that of ϕ persists up to the L^* examined with the amplitude of the wave (coefficient of the sine term) diminishing slowly. It would be interesting to see the decay of the wave up to a long L^*. So the second term in Eq. (2b) is plotted for L^* up to 35 in Fig. 8(c). Now it is conspicuous that the influence of ϕ persists up to $L^* = 25$ that is 4 times larger than that for L^* influence. Note that the peak-to-peak period of the wave is found to be $\Delta L^* = 3.8$, 4.46, 4.38, 4.28 and 4.27 for the first, second, third, fourth and fifth periods, respectively. The period is smaller in the first period ($L^* = 3.65$ - 7.5) and decreases from the second period, reaching it asymptotic value at the fifth period at $L^* = 25$. The observation again suggests that the relationship between ϕ and L^* is non-linear in the first period, i.e., up to $L^* \approx 7.5$.

The degree of the C_{Lf}-amplitude decay with L^* at n-th period can be expressed in a form of logarithmic decrement,

$$\delta_n = \ln \frac{(A_{C_{Lf}})_n}{(A_{C_{Lf}})n+1}, \text{ where } A_{C_{Lf}} \text{ is the amplitude of } C_{Lf}. \quad (3a)$$

$$\delta_n = \ln \frac{0.036e^{-0.2L_n^*}}{0.036e^{-0.2L_{n+1}^*}} = \ln e^{0.2(L_{n+1}^* - L_n^*)} = 0.2\Delta L^* \quad (3a)$$

Following Eq. (3) and Fig. 8(c), δ is estimated to be $\delta_1 = 0.75$, $\delta_2 = 0.89$, $\delta_3 = 0.87$, $\delta_4 = 0.86$ and $\delta_5 = 0.85$. δ is almost constant after the first period. As we know, by definition, logarithmic decrement is the number of oscillations during which amplitude is reduced by a factor of *e*.

As we mentioned before the influence of ϕ weakens as L^* becomes longer. How the ϕ influence decays with L^* can now be specified by damping ratio $\zeta = \frac{1}{\sqrt{1+(\frac{2\pi}{\delta})^2}}$. Assuming δ is constant of about ≈0.85, we can get $\zeta = 0.13$, much smaller than 1.0, underdamped. That is why, ϕ can influence C_{Lf} for a longer L^* than L^* itself. Note that the decay of C_{Lf} induced by L^* alone is exponential without a wave, meaning that $\zeta \geq 1.0$, critical or overdamped. Now it can be summarized that, the L^* effect on flow interaction is critical or overdamped with an increase in L^*, and the ϕ effect is underdamped. The corollary suggests that when two bodies are in tandem, ϕ plays a significant role on the lift of the upstream cylinder and its role prevails for a longer L^*.

It is worth pointing out that airplanes/submarines and many fishes have wings in tandem. C_{Lf} generated on the front wing may generate unwanted wing vibration and/or noise, reducing the fatigue life or service lift of the wing. The streamwise separation between two wings might be taken into account and optimized in engineering. An investigation on two elastic tandem airfoils would be interesting to the see the flow-induced response of the airfoils at inphase and antihase conditions depending on the streamwise spacing between them. On the other hand, fish generates forward thrust from the oscillation of their wings. The fish may need less power for the oscillation in the case of the inphase shedding. It would be interesting whether fish exploit this technique as most creatures are naturally optimized. Note that the wings for either case may not be exactly tandem, but still the mechanism can succeed.

9. Discussion

A shear layer shedding or growing is accompanied by a higher velocity and lower pressure in the shear layer. When a shear layer from the downstream cylinder grows/accelerates, it, because of the low pressure, pulls the fluid at the same side of the upstream cylinder and tends to accelerate the flow/shear-layer on the side. A sketch is provided in Fig. 9, reflecting the overall picture of ϕ influence on the flow. For inphase sheddings of the two cylinders (Fig. 9a), the growing shear layer from the lower side of the downstream cylinder accelerates the same side shear layer on the upstream cylinder. In the next half cycle, the other side shear layer will accelerate. The alternating acceleration of the two shear layers of the upstream cylinder results in an enhanced C_{Lf}. When the sheddings change from inphase to antiphase, the velocity in the growing shear layer of the upstream cylinder reduces and that in other side increases, which leads to a decay in C_{Lf} with L^*. At antiphase (Fig. 9b), the growing shear layers of the two cylinders are in opposite sides. The growing shear layer of the downstream cylinder, therefore, accelerates the flow in the non-growing shear layer of the upstream cylinder, which results in a minimum C_{Lf}. The larger the L^*, the smaller the influence of ϕ or pulling effect, as a larger L^* corresponds to a greater amount (mass) of fluid between the same-side shear layers of the cylinders. ϕ effect on the downstream cylinder C_{Lf} is negligible or very small, because the downstream cylinder is submerged in a highly turbulent flow and has very wider shear layers. In other words, the momentum fluctuation in the upstream-cylinder shear layer is distributed over the wide shear layer of the downstream cylinder; the fluctuation in momentum around the downstream cylinder is thus very less or negligible.

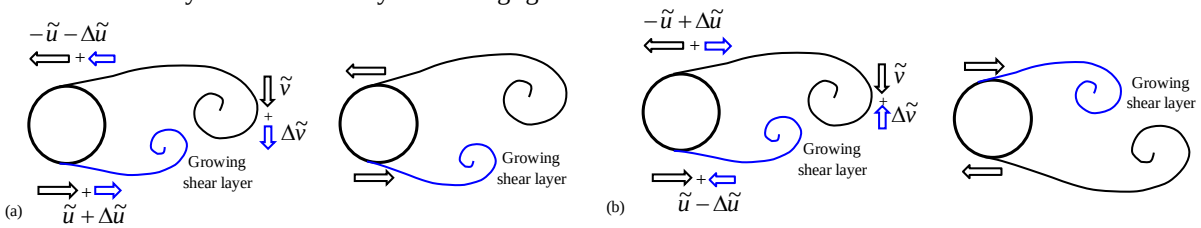

Fig. 9. Sketches showing the effect of shedding phase lag on the flow around and behind the upstream cylinder. (a) Inphase flow, and (b) antiphase flow.

10. Conclusions

Mean flow parameter $\bar{u}^*_{max}$ increases exponentially with L^*. The downstream cylinder at a smaller L^* obstructs the flow around and behind the upstream cylinder. A larger L^* thus increases the flow around the upstream cylinder, enables a greater flow from the freestream sides into the wake, and enhances recirculation in the wake bubble. All these contribute to the increase in $\bar{u}^*_{max}$ with L^*. While the shear layer thickness of the upstream

cylinder is narrow, that of the downstream cylinder is very wide. The ϕ effect on the downstream cylinder C_{Lf} is negligible or very small because the downstream cylinder is submerged in a highly turbulent flow and has very wider shear layers.

Upstream cylinder C_{Lf} variation with L^* in the coshedding regime is a sine curve with decaying in amplitude, influenced by L^* and ϕ. The L^* effect causes an exponential decrease in C_{Lf} with L^*, while the ϕ effect makes the C_{Lf} variation sinusoidal. C_{Lf} variation with L^* is therefore composed of two, one associated with L^* and other associated with ϕ . Local maximum and minimum of C_{Lf} occur when the shear layer sheddings of the two cylinders are inphase ($\phi = 2n\pi$, n = 1, 2, 3 …) and antiphase ($\phi = (2n+1)\pi$), respectively. At inphase flow where shear layers grow from the same side of the two cylinders, the growing shear layer of the downstream cylinder, having a low pressure, pulls the same-side growing shear layer of the upstream cylinder. Velocity in the same-side shear layer of the upstream cylinder thus increases. In the next half cycle of the vortex shedding period, the velocity in the other-side shear layer is enhanced. C_{Lf} therefore becomes maximum at inphase flow. For antiphase flow where shear layers grow from the opposite sides of the two cylinders, the growing the shear layer of the downstream cylinder pulls the non-growing shear layer of the upstream cylinder, reducing the lift induced by the growing shear layer of the upstream cylinder. Minimum C_{Lf} thus prevails for antiphase flow. The pulling effect weakens at a larger L^*, as a greater amount (mass) of fluid lies between the two same-side shear layers. The amplitude of the sinusoidal variation of C_{Lf} thus diminishes with L^*.

In the literature, it was known that ϕ *i*s a linear function of L^*. The present investigation identifies that it is non-linear at least L^* = 7.5, following $\phi = 2\pi\{1+\frac{St}{\overline{V}_c / U_\infty}(L^* - L_c^*)\}$. The ϕ is a function of L^*, St and $\overline{V}_c$, influencing the fluctuating component of the flow around and behind the upstream cylinder significantly. When ϕ changes from inphase to antiphase with variation in L^*, the streamwise velocity increases in the upper shear layer of the upstream cylinder and the downward flow by the upper shear layer reduces. The opposite phenomenon is afoot when antiphase evolves into inphase. The effect of L^* and ϕ on C_{Lf} is also extracted from a curve fitting of C_{Lf}. An equation of C_{Lf} is deduced as $C_{Lf} - C_{Lf0} = Ae^{-\alpha L^*} + Be^{-\beta L^*}\sin(\phi + \frac{\pi}{2})$.

The influence of ϕ persists up to L^* = 25 that is 4 times larger than that for L^* influence. The decay of C_{Lf} induced by L^* alone is exponential without a wave, associated with a critical or overdamped interaction. On the other hand, ϕ results in sinusoidal variation in C_{Lf}, yielding an underdamped interaction.

11. Acknowledgments

Alam wishes to acknowledge supports given to him from the Research Grant Council of Shenzhen Government through grants KQCX2014052114423867 and JCYJ20120613145300404.

12. References

[1] M.M. Zdravkovich, "The Effects of Interference between Circular Cylinders in Cross Flow", *Journal of Fluids and Structures*, Vol. **1**, 239-261, 1987.

[2] M.M. Alam, M. Moriya, K. Takai, and H. Sakamoto, "Fluctuating Fluid Forces Acting on Two Circular Cylinders in a Tandem Arrangement at a Subcritical Reynolds Number *Journal Wind Engineering and Ind*ustrial *Aerodyn*amics, Vol. **91**, 139-154, 2003.

[3] M.M. Alam, "The Aerodynamics of a Cylinder Submerged in the Wake of Another', *Journal of Fluids and Structures*, Vol. **51**, 393-400, 2014.

[4] M.M. Alam, H. Sakamoto, and Y. Zhou, "Effect of a T-shaped Plate on Reduction in Fluid Force on Two Tandem Cylinders in a Cross-Flow", *Journal Wind Engineering and Ind*ustrial *Aerodyn*amics, Vol. **94**, pp. 525-551, 2006.

[5] M. Zhao, C. Liang, B. Teng, and D. Liang, "Numerical Simulation of Viscous Flow Past Two Circular Cylinders of Different Diameters", *Applied Ocean Research*, Vol. **27**, pp. 39-55, 2005.

[6] T. Farrant, M. Tan, and W.G. Price, "A Cell Boundary Element Method Applied to Laminar Vortex Shedding from Circular Cylinders". *Computer and Fluids*, Vol. **30**, pp. 211–236, 2001.

[7] N. Mahir and Z. Altac, "Numerical Investigation of Convection Heat Transfer in Unsteady Flow Past Two Cylinders in Tandem Arrangements", *International Journal of Heat and Fluid Flow*, Vol. **29**, pp. 1309-1318, 2008.

[8] Y. Koda, and F.S. Lien, "Aerodynamic Effects of the Early Three-Dimensional Instabilities in the Flow over One and Two Circular Cylinders in Tandem Predicted by Lattice Bolzmann Method", *Computers and Fluid*s, Vol. **74**, pp. 32-43, 2013.

[9] C.H.K. Williamson, " 2-D and 3-D Aspects of the Wake of a Cylinder, and Their Relation to Wake Computations", Lectures of Applied Mathematics, Vol. **28**, pp.719-751, 1991.

[10] M.M. Alam, Y. Zhou, Y., and X.W. Wang, "The Wake of Two Side-by-Side Square Cylinders", *Journal of Fluid Mech*anics, Vol. **669**, pp. 432-471, 2011.